Remote Sensing of Environment 313 (2024) 114341

Contents lists available at ScienceDirect

Remote Sensing of Environment

journal homepage: www.elsevier.com/locate/rse

Exploring the potential of Aeolus lidar mission for ocean color applications

Davide Dionisi [a,*], Simone Bucci [b], Claudia Cesarini [a], Simone Colella [a], Davide D'Alimonte [c], Lorenzo Di Ciolo [b], Paolo Di Girolamo [d], Marco Di Paolantonio [a,d], Noemi Franco [d], Giacomo Gostinicchi [b], Giovanni Giuliano [a], Tamito Kajiyama [c], Emanuele Organelli [a], Rosalia Santoleri [a], Gian Luigi Liberti [a]

[a] Institute of Marine Sciences (ISMAR), Italian National Research Council (CNR), Rome - Tor Vergata, Italy
[b] Serco Italy S.p.a, Rome, Italy
[c] AEQUORA, Lisbon, Portugal
[d] School of Engineering, University of Basilicata, Potenza, Italy

ARTICLE INFO

Editor: Dr. Menghua Wang

ABSTRACT

The Atmospheric Laser Doppler Instrument (ALADIN) onboard the Aeolus wind mission was the first High Spectral Resolution Lidar operating in the Ultra Violet (UV) region deployed in space. This study explores and documents the feasibility of deriving ocean optical properties using data from ALADIN. A three steps (i.e. data screening, analytical estimation of the total in-water signal contribution, Look Up Table-based estimation of the in-water attenuation) retrieval algorithm was developped combining data analysis and signal simulations from a radiative transfer model. The algorithm has been implemented using the signal acquired by the Mie channel, and tested for 1-year of Aeolus observations. This approach allowed estimating the first Aeolus derived Ocean Color (OC) products in terms of the total in-water signal contribution and the in-water attenuation term in a spectral region (355 nm) not covered, during Aeolous lifetime, by operational OC products. The validation process involved comparing these products with both Biogeochemical-Argo (BGC-Argo) field measurements and satellite OC dataset distributed by ESA Ocean Color Climate Change Initiative across a set of 7 selected oceanic regions representing diverse open-ocean scenarios. These validation exercises attested the general accordance between OC reference measurements and the proposed Aeolus OC parameters. Thus, this study was able to provide statistical evidence of the sensitivity of the retrieved Aeolus in-water lidar attenuation term to the CDOM variability on a temporal/seasonal and spatial/regional basis. A preliminary estimation of the uncertainty associated to the retrieved quality controlled K_{lid}, was performed assuming the radiometric noise as unique source of uncertainty. As a result, a median/average value of absolute relative percent difference of about 50/80% was obtained. Limits of the developed technique, possible improvements, potential adaptation to planned/future space lidar missions are discussed.

1. Introduction

Lidar techniques have demonstrated their high reliability as a valuable tool for studying the marine environment (Churnside, 2013). During the last decade, several Ocean Color (OC) studies using space-borne lidar measurements not only provided the initial space-based proof of concept but also generated noteworthy scientific findings (e.g., Behrenfeld et al., 2013, 2019; Dionisi et al., 2020; Lu et al., 2020, 2021, 2022, 2023; Vadakke-Chanat and Jamet, 2023; Watkins et al., 2023; Yang et al., 2023; Zhang et al., 2022, 2023a, 2023b, 2024). These results gave a glimpse of a "new lidar era in satellite oceanography" (Hostetler et al., 2018).

The Atmospheric Laser Doppler Instrument (ALADIN, Stoffelen et al., 2005), launched in 2018 onboard the Aeolus orbiting platform within ESA's Atmospheric Dynamics Mission (ADM) and decommissioned in April 2023, had the objective to provide novel observations of global wind profiles using its Doppler Wind Lidar at 355 nm. Notably, ALADIN has been the only space-borne lidar operating in the UV since the LIdar Technology Experiment (LITE) pioneering mission launched onboard the Discovery Space Shuttle in 1994 (Winker et al., 1996). Although

* Corresponding author.
E-mail address: davide.dionisi@cnr.it (D. Dionisi).

https://doi.org/10.1016/j.rse.2024.114341
Received 26 February 2024; Received in revised form 1 July 2024; Accepted 26 July 2024
Available online 9 August 2024

Aeolus's mission primary objectives and subsequent instrument and sampling characteristics are not ideal for monitoring sub-surface ocean properties, its unprecedented type of measurements is expected to contain relevant and original information about the optical properties of the sensed water volume. Specifically, ALADIN presented unique opportunities to examine the information in the signal back-scattered and attenuated by sub-surface components of the ocean at 355 nm.

At 355 nm, light is attenuated (i.e., absorbed) mostly by the Colored Dissolved Organic Matter (CDOM). The light absorption coefficient of CDOM is due to a mixture of molecules originating through phytoplankton digestion as operated by heterotrophic bacteria (Nelson et al., 1998) or active release by phytoplankton itself (Organelli and Claustre, 2019). These molecules are ubiquitous in aquatic ecosystems and play an important role in Earth's climate (Kim et al., 2018).

Besides the contribution from accurate but very sparse in-situ observation (cruises), current knowledge of the global distribution of CDOM light absorption coefficients and of its temporal variability is mainly based on a limited set of satellite products in the visible light (Nelson and Siegel, 2013). Due to the design of the current/past generation of OC dedicated missions, information on CDOM light attenuation from space at a wavelength shorter than 400 nm is achieved, in the majority of the cases, assuming a dependency on Chl-a concentration (e.g., Morel et al., 2007) or through empirical, semi-analytical and deep-learning-based approaches starting from OC remote sensing reflectance (Lee et al., 2013; Wang et al., 2021; and references therein). Recently, Oelker et al. (2022) has also explored the information content in the UV bands of TROPOspheric Monitoring Instrument (**TROPOMI**), on board the Copernicus Sentinel-5 Precursor satellite, to obtain vertical diffuse attenuation coefficient (K_d) products that can be used as a proxy of CDOM in the UV.

Recognizing the importance of the information in the UV regions, the coming generation of OC satellite missions (e.g., Li et al., 2022; Plankton, Aerosol, Cloud, ocean Ecosystem mission, PACE, Werdell et al., 2019) extends the range to wavelengths below 400 nm. In the field, recent advances in understanding the spatio-temporal variability of K_d in the UV, at the global scale, have been achieved thanks to radiometric measurements acquired in-situ by autonomous robotic Biogeochemical-Argo (BGC-Argo) profiling floats (Organelli et al., 2017).

This study aims to investigate ALADIN Lidar capabilities to provide information on seawater optical properties in the UV with particular attention to CDOM measurements. To verify if and in which terms the standard ocean lidar retrieval algorithms (Churnside, 2013; Jamet et al., 2019) can be applied to the ALADIN instrumental and sampling characteristics, signal simulations with a radiative transfer model (D'Alimonte et al., 2024) and data analysis were conducted. The former activity was essential to simulate the radiative processes generating Aeolus *surface bin* signal, the latter allowed for selecting an Aeolus dataset suitable to be analysed. These tools enabled the design of an inversion method for retrieving the first Aeolus-derived OC products in terms of the total in-water signal contribution and attenuation term for one year of Aeolus measurements in different ocean regions, representing the expected global variability of the ocean color parameters of interest. To interpret and assess these products and to demonstrate their sensitivity to ocean optical properties and CDOM measurements, both in-situ measurements deployed by BGC-Argo and standard satellite OC-derived product provided by the Ocean Color Climate Change Initiative of ESA were used (ESA-OC-CCI; esa-oceancolour-cci.org).

The outline of this study is organized as follows: Section 2 gives a brief description of the datasets analysed in the study; Section 3 describes the radiative transfer model (LiOC) used to support and develop the retrieval algorithm; Section 4 explores the suitability of applying the standard ocean lidar equation to the instrumental characteristics of ALADIN and describes the developed inversion algorithm to retrieve a first prototype of Aeolus-OC products; Section 5 shows the results of the assessment of the obtained products and the analysis of the associated uncertainty. Finally, Section 6 summarizes the approach developed, the main results obtained, and their limitations, and discusses the applicability of this approach to future space lidar missions.

2. Data

2.1. ALADIN

The Aeolus mission carries the ALADIN instrument, the first spaceborne High Spectral Resolution Lidar (HSRL) emitting pulses of about 60 mJ with a repetition frequency of 50.5 Hz at 355 nm. Designed with the primary scientific goal of providing wind profiles using the Doppler effect, this instrument points perpendicular to the satellite ground speed vector with a slant angle 35° off nadir. Back-scattered laser radiation is collected by a Cassegrain telescope of 1.5 m in diameter with a field-of-view (FOV) of 20 μrad, and it is directed to Fizeau and dual Fabry-Perot interferometers that allow retrieving separately back-scattering signals from aerosols and molecules (Mie and Rayleigh channels, respectively). Aeolus has a 06:00 and 18:00 local solar time (LST) Equator overpass in a polar, sun-synchronous orbit at a mean altitude of 320 km with a 7-day repeat cycle. The vertical resolution of ALADIN measurements varies between 250 m and 2 km from the ground up to 30 km, corresponding to 24 range bins used for atmospheric return measurements and 1 bin for the background light contribution (Reitebuch et al., 2009). Each vertical range bin is integrated to obtain two different horizontal resolutions of approximately 3 and 90 km, referred to as 'measurement' and 'observation' levels, respectively.

The Aeolus dataset can be accessed and downloaded through various options on ESA's Aeolus portal (https://earth.esa.int/eogateway/missions/aeolus/data, last access: 26/06/2024). One year of L1B Aeolus product (baseline 11) was used for this study. In particular, the L1B 'measurement' resolution dataset from June 2020 to May 2021 was extracted for seven oceanic Region of Interests (RoIs): North and South Atlantic subtropical gyres (NASTG and SASTG, respectively), North Atlantic subpolar gyre (NASPG), South Eastern Mediterranean Sea (SEMED), North Western Mediterranean Sea (NWMED), Southern Ocean – Indian Sector (SOIND), Black Sea (BLSEA). These regions have been selected to represent the expected global variability of the OC parameters of interest (e.g., *Kd*, and CDOM absorption) and meet diverse meteorological conditions (e.g., cloudiness) that could impact Aeolus's data availability and retrievals.

2.2. Biogeochemical-Argo dataset

Biogeochemical-Argo (BGC-Argo) floats are autonomous robotic platforms that acquire profiles, up to every 10 days, of several optical, biogeochemical and physical variables from 0 to 2000 m depth. In particular, BGC-Argo floats are equipped with miniaturized Seabirds OCR-504 radiometers that sample, around solar noon, 0–250 m profiles of downwelling irradiance at three wavelengths (380, 412, and 490 nm) and Photosynthetically Available Radiation (PAR) integrated between 400 and 700 nm. These profiles are freely distributed by Coriolis Global Data Assembly Centre (ftp://ftp.ifremer.fr/ifremer/argo/dac/coriolis/, last access: 26/06/2024; Argo float data and metadata from Global Data Assembly Centre (Argo GDAC), 2023).

Acquired radiometric profiles were quality-controlled following (Jutard et al., 2021). Then, automatic quality-control protocol specifically developed to identify clouds and wave focusing/defocusing, and to disregard profiles acquired under unfavourable sky and sea conditions was applied (Organelli et al., 2016). Then, K_d coefficients within the first optical depth (Zpd) were calculated as reported by (Organelli et al., 2017). In Table 1, we report the main characteristics of $K_d(380)$ coefficients computed for the seven ROIs used for the validation datasets depicted in Fig. 1.

Table 1
Main characteristics of the $K_d(380)$ dataset within the First Optical Depth (Zpd) for the 7 ROIs.

ROI	Latitudinal range (upper-lower limit) (°)	Longitudinal range (western-eastern limit) (°)	Period	# of Q/C $K_d(380)$ within the first optical depth	Average $K_d(380) \pm$ standard deviation (m^{-1})	Min/Max $K_d(380)$ (m^{-1})	Average $Z_{pd} \pm$ standard deviation (m)
NASTG	26 N–16 N	55 W–30 W	2012–2018	381	0.04 ± 0.009	0.02/0.08	23 ± 3
SASTG	14S–22S	33 W–19 W	2012–2022	434	0.03 ± 0.007	0.02/0.06	28 ± 3
NASPG	66 N–53 N	61 W–15 W	2013–2021	2529	0.15 ± 0.057	0.05/0.55	11 ± 5
SEMED	38 N–30 N	22E-35E	2013–2022	1048	0.06 ± 0.020	0.02/0.13	20 ± 3
NWMED	44 N–39 N	0-9E	2012–2021	1299	0.10 ± 0.039	0.02/0.29	13 ± 4
SOIND	40S–60S	40E-110E	2014–2022	3043	0.08 ± 0.027	0.03/0.29	16 ± 4
BLSEA	47 N–41 N	27E-42E	2013–2022	524	0.31 ± 0.065	0.13/0.67	8 ± 2
TOTAL				**9258**			

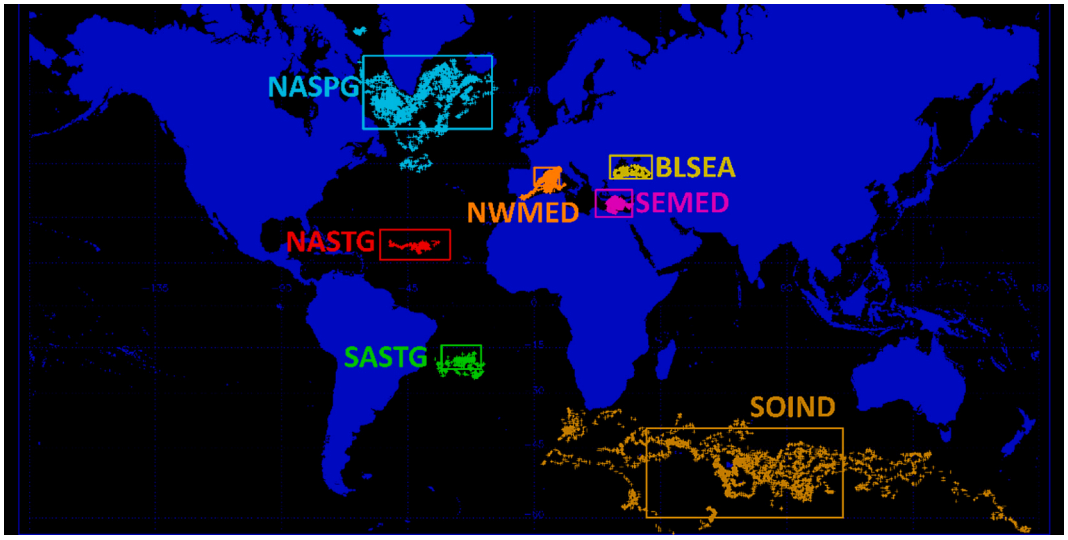

Fig. 1. Region of Interests used for the validation datasets and the position of the BGC-Argo measurements.

2.3. ESA-OC-CCI dataset

The ESA-OC-CCI dataset consists of daily satellite data with 4 km of spatial resolution and cover a period spanning from 1998 to 2023 (ESA-OC-CCIv6; esa-oceancolour-cci.org). Products are freely distributed at a global scale as a multi-sensor result derived from different merging techniques (https://climate.esa.int/en/projects/ocean-colour/key-documents/, last access: 29/06/2024). The ESA-OC-CCI products are described in Sathyendranath et al. (2019).

Different variables contained in this dataset are used in different phases of this study:

- as ancillary data, Chlorophyll concentration (*Chl-a*) and associated uncertainty is used as input, in addition to P_n^w in the LUT to estimate K_{lid} (Section 4.2);
- as reference for the product validation, the absorption of the Colored Detrital Matter (a_{cdm}) is used for the validation of the results (Section 5.2).

The uncertainty associated to each single pixel *Chl-a* observation is given as a root-mean-square difference (*RMSD*) and Bias of Log_{10}Chl from which a standard deviation can also be computed (https://docs.pml.space/share/s/fzNSPb4aQaSDvO7xBNOCIw, access: 29/06/2024). RMSD and Bias are estimated on the basis of results from match-up in-situ data and optical water class estimation based on OC-CCI remote-sensing reflectance spectra (Rrs) for each pixel (doi:https://doi.org/10.1016/j.rse.2017.03.036).

The absorption of the Colored Detrital Matter (a_{cdm}), used for the validation (see Section 5.2), results from the application of the Quasi-Analytical Algorithm (QAA v6) model (Lee et al., 2002) that derives the absorption and back-scattering coefficients by analytically inverting the spectral remote-sensing reflectance ($R_{rs}(\lambda)$). Component absorption coefficients (contributions by detritus/CDOM and phytoplankton pigments) are further algebraically decomposed from the total absorption spectrum. a_{cdm} provided by ESA-OC-CCI is available at 6 bands: 412, 443, 490, 510, 560, and 665 nm.

3. LiOC model

The Lidar Radiative Transfer Simulation code for Ocean Color applications (LiOC) is used in this study to analyze the dynamics of the signal retrieved by ALADIN ADM-Aeolus from the ocean and verify the possibility of deriving OC data products (see D'Alimonte et al., 2024 for details). In summary, LiOC simulates the ALADIN ADM-Aeolus measurements in terms of the back-scattered signal $P^T = P^s + P^w + P^b$, from the lidar sensed water volume where:

- P^s: is originated by reflection processes in the presence of wind-driven sea-surface waves,
- P^w: results from the absorption and multiple scattering events in a water volume,
- P^b: is due to reflection at the of the sea bottom.

Since the absolute value of ALADIN ADM-Aeolus measurements depends on the instantaneous laser emission power, the ratio of the above quantities and the sea surface incident signal P (i.e., $P_n^x = P^x/P$, where $x = T,s,w,b$) is then used for comparison between simulation results and actual measurements.

The in-water LiOC simulation component relies on Monte Carlo ray tracing (Fig. 2) to determine profiles of the back-scattered signal as a function of depth and scattering order. This capability has allowed verifying that, in the ALADIN ADM-Aeolus measurement case, the in-water lidar attenuation coefficient K_{lid} approaches the beam attenuation coefficient c in oligotrophic waters, while it converges to K_d in turbid waters (D'Alimonte et al., 2024). The resulting K_{lid} variability poses a limit to deriving the back-scattered signal directly from the lidar equation, implying the need for radiative transfer simulations tailored to the ALADIN ADM-Aeolus measurement geometry. LiOC simulation results also allowed the identification of the "expected" conditions where the lidar signal can be informative of optically active seawater constituents. The bottom contribution of the ground bin signal can be neglected when $z_b \geq 100$ m even for Chl-a concentrations typical of oligotrophic regions (≈ 0.01 mg m^{-3}). Furthermore, given the geometry of the ALADIN observation (nadir angle of 35°), the sea surface contribution is assumed as negligible for wind speeds <8 ms^{-1}. This assumption is not applicable to other lidar measurements with smaller off-nadir angle.

The considered marine conditions include Inherent Optical Properties (IOPs) driven by Chl-a and independent absorption sources of varying relevance (e.g. CDOM). In contrast, the simplified assumption that suspended particles not covarying with Chl-*a* do not have a significant impact on the variability of the lidar back-scattered signal is adopted as a specific case study. This marine bio-optical regime has been considered in a set of LiOC simulation runs to create a Look-Up-Table (LUT) for retrieving K_{lid} from Chl $-$ *a* and P_n.

Finally, to verify the capability of LiOC in reproducing the marine lidar signal (P_n^w), LiOC simulation results are statistically compared against the equivalent quantity retrieved from ALADIN ADM-Aeolus measurements (see Section 4). To this end, Fig. 3 shows three curves representing the relationship between the simulated P_n^w, and the Chl-*a* concentration. CDOM contribution is also included, assuming a spectral slope as in Pitarch (2017). The green curve is the one obtained with the Monte Carlo simulations, and the other two curves are the two extreme analytical solutions used for the validation discussed in D'Alimonte et al., 2024.

The shaded boxes show the variability derived from observations. Each symbol refers to the selected ROIs representing different regimes regarding marine bio-optical properties (see Fig. 1). Chl-a concentration statistics are derived from the BGC-Argo dataset (symbols in Fig. 3) that has been used for statistical comparison with the Aeolus-derived CDOM estimates. The statistics relative to the LiOC simulated signal (P_n^w) are obtained from processed L1B Aeolus observations (i.e., one-year data records) following the procedure described in Section 4. Results of Fig. 3 support an overall agreement between Aeolus-derived and LiOC estimated P_n^w for the different bio-optical regimes selected to represent the global variability.

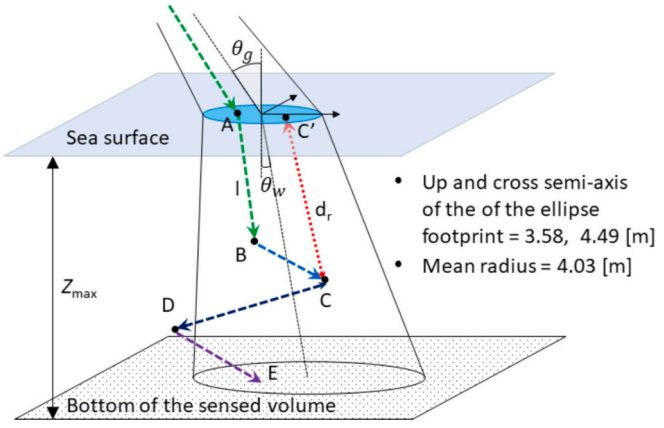

Fig. 2. Representation of Monte Carlo ray-tracing approach implemented in LiOC to model the fraction of the Aeolus laser beam back-scattered by the sea and collected at the receiver. Dots labelled as B, C and D represent scattering events. The CC' lines represent the contribution to back-scattered signal that can be measured by ALADIN ADM-Aeolus.

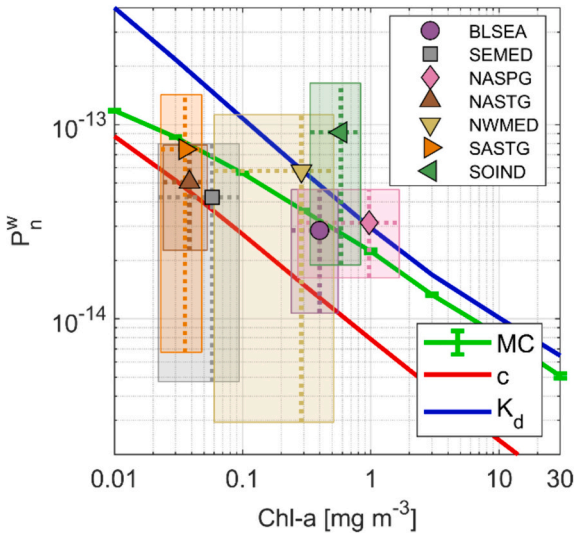

Fig. 3. Normalized marine water contribution to the lidar signal P_n^w as a function of Chl-a concentration. Green line: MC simulations. Red and blue lines: analytical limiting cases. Each symbol shows the parameters' variability range for a given ROI. Chl-*a* is derived from BGC-Argo measurements (https://biogeochemical-argo.org/), P_n^w is estimated from Aeolous L1B data. (For interpretation of the references to color in this figure legend, the reader is referred to the web version of this article.)

4. Aeolus-OC algorithm

Due to the ALADIN characteristics (i.e., emission of circular polarized light at 355 nm and reception of the elastic and Doppler shifted back-scattered signals through a fringe-imaging and a double-edge channels), HSRL and Elastic Back-scattering Lidar (EBL, Churnside, 2013; Jamet et al., 2019) retrieval techniques, could be theoretically applied to the Aeolus ocean sub-surface signal.

The HSRL approach is already applied to Aeolus measurements to retrieve atmospheric aerosols back-scatter and extinction coefficient profiles in the Aeolus L2A spin-off products (Flament et al., 2021). To use this approach, it is necessary to calibrate the six instrumental coefficients, K_{ray}, K_{mie}, C_1, C_2, C_3 and C_4, which appear in the two range-resolved lidar equations for the Rayleigh and Mie signals (Eqs. 6.5 and 6.6 in Flamant, et al., 2021, respectively). These coefficients, provided in L2A and L2B Aeolus dataset, are calibrated according to Dabas (2017), considering the spectral transmissions of the Fizeau and dual Fabry-Perot spectrometers and the atmosphere as the medium in which the scattering processes take place.

To apply the HSRL approach to OC studies, the values of the aforementioned instrumental coefficients must be computed considering the scattering process occurring in the water (e.g., Brillouin scattering). This estimation goes beyond the scope of this work as, similarly to the aerosol application (Dabas, 2017), it should involve not only the theoretical computation of these values but also the analysis of the acquired Aeolus signal during the Instrument Response Calibration mode of Aeolus.

Furthermore, the Aeolus Rayleigh signal is affected by a dependency on the M1 (primary) mirror temperatures that cause a Rayleigh wind bias (Weiler et al., 2021). Currently, the Level-1B product does not include a correction for this bias, which is corrected at Level-2B. Finally, the Rayleigh ground bin signal is characterized by a low Signal-to-Noise Ratio (SNR).

Conversely, the Mie channel sensitivity to M1 mirror temperature gradients appears to be around a factor ten less than the Rayleigh

channel (Rennie and Isaksen, 2020). Additionally, the computed analysis of the Aeolus signal highlights that the Mie signal has a higher SNR compared to the Rayleigh signal.

For the above considerations, the study is based only on the Mie channel dataset, not exploiting the HSRL capability.

The designed EBL approach to derive in-water optical properties using Mie channel measurements is based on an inversion scheme that consists of three consecutive phases:

1) Screening procedure: aimed to identify the filtering criteria to be applied to the Aeolus data for the OC inversion algorithm.
2) Estimation of the in-water ground bin signal contribution: aimed to remove contributions to the measured signal from variables other than the in-water ones;
3) Retrieval of the optical properties of the in-water ground bin: aimed to determine the in-water optical properties of interest.

These steps are described in the following sub-sections. Fig. 4 resumes the flowchart of the implemented Aeolus-OC algorithm based on the developed approach.

4.1. Screening procedure

To select suitable Aeolus measurements to be inverted into the OC algorithm, an analysis of the 5 lowermost Aeolus profile acquisition bins (i.e., bins 21–25, see.

Fig. 5) was performed to identify the atmosphere-ocean interface bin (hereinafter referred to as 'ground bin') and develop a filtering procedure to remove cloud/aerosol contamination.

In the large majority of the cases (≈98%), bin 23 is the ground-bin. Fig. 6 shows the histogram of the lower height of #23 bin with the negative values indicating the depth below the sea surface. For the sea surface topography, it has been used the ACE2 (Altitude Corrected Elevation 2) as a global DEM (Digital Elevation Model). This information is included in the Aeolus L1B data.

The developed quality control and data screening procedure aims to remove low-quality observations and those for which the contribution to the signal from geophysical factors (clouds/aerosol, bathymetry, and surface reflectance) other than marine optical properties compromise the assumptions adopted in the inversion algorithm. This procedure takes advantage of: LiOC simulation results, the statistical analyses

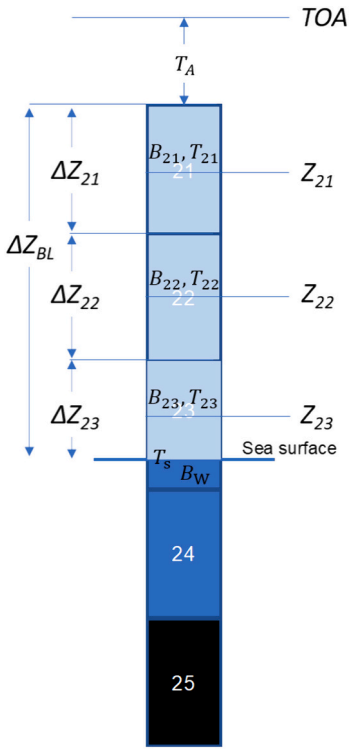

Fig. 5. Schematic view of the five lowermost Aeolus profile acquisition bins (21–25). Please note that, for simplicity, the figure represents a nadir profiling scheme.

based on procedures on the SNR, and the *useful signals* (Reitebuch et al., 2018) of the Mie channel for bins 21, 22 and 23. The screening is applied according to the following criteria:

1) Dummy values. Unphysical negative values deriving from an overestimation of the background are flagged.
2) Bathymetry. In order to avoid the potential contribution from the sea bottom surface, observations corresponding to shallow waters (bottom depth < 100 m) are flagged. The bathymetry mask is obtained from GEBCO gridded bathymetry data (https://www.gebco.net/).

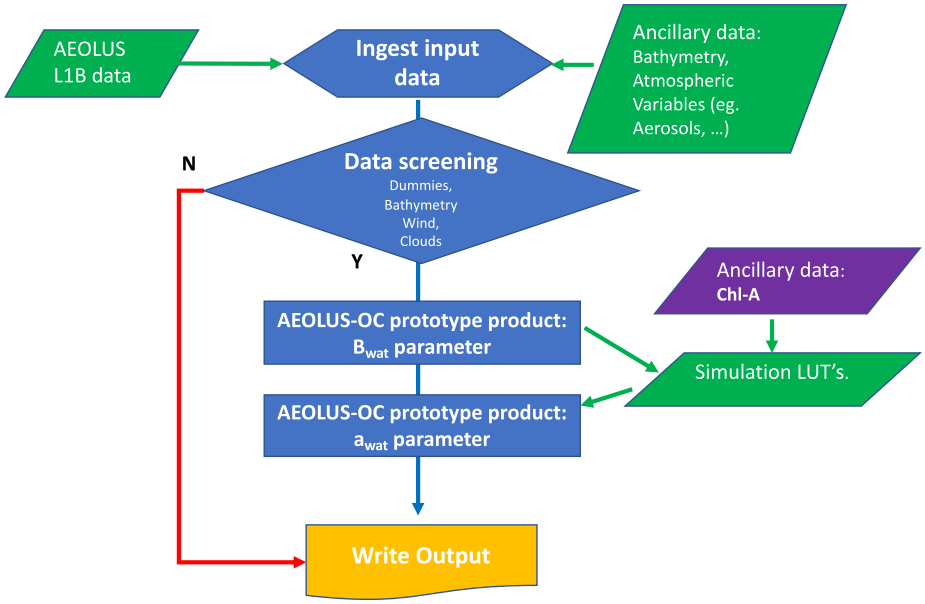

Fig. 4. Flow-chart of the Aeolus-OC algorithm developed in this study.

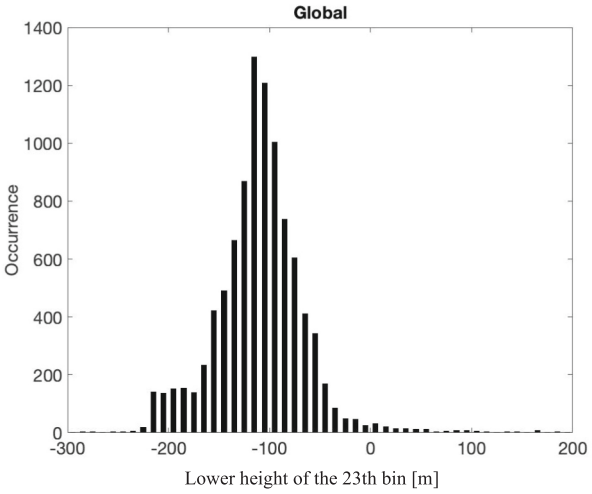

Fig. 6. Histogram of the lower height for the 23 bin computed for the June–July-Aug 2020 Aeolus L1B dataset.

The original resolution of 15 arc-second geographic latitude and longitude grid is interpolated on the Aeolus data L1B resolution.

3) In-water bin 23 (shallow or deep-water bin). Data with ground bin lower edge altitude outside of the range − 70 m to −500 m are flagged. This is imposed to ensure that the ground bin contains both the atmosphere and the ocean.
4) Wind. Surface roughness, mostly associated with sea surface wind, increases the sea surface reflectance contribution in the ground bin. Based on the analysis done with the LiOC simulation tool (see Section 3), only data with wind intensity lower than 8 m/s are considered to ensure a negligible signal contribution due to the surface reflectance and a constant sea surface transmittance. Ancillary data provided by Aeolus AUX_MET files contained in the L1B dataset is used for wind speed at the surface. In this condition, the effects of white caps and foam may be neglected.
5) Low Mie channel SNR on bins 21, 22 and 23 (ground bin). To remove the noisy signal, SNR should be higher than a low bound value (SNR_{low}) fixed to 5.
6) High Mie channel SNR on bins 21, 22 and 23 (ground bin). To exclude the bins affected by cloud and high aerosol load contamination, a high bound value (SNR_{high}) is determined based on the SNR density distribution estimated for each selected ROI dataset. Precisely, the SNR_{high} corresponds to the right bound of the full-width half maximum (FWHM) of the region specific SNR distribution (see Fig. 7).
7) Useful Mie channel signal on bins 21, 22 and 23 (ground bin). To further remove cloud and aerosol contamination, a high bound signal value (SIG_{high}) is also used. The same procedure developed for the SNR_{high} is applied to determine SIG_{high} by calculating the FWHM of the signal density distribution.

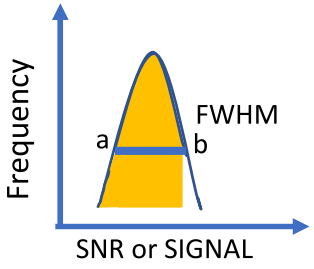

Fig. 7. Density distribution analysis of both the SNR and the signal of bin 21, 22 and 23 to flag high values. The right bound of the full-width half maximum (FWHM) of the density distribution estimated for each selected test area is used as a high bound value.

This screening procedure allows the removal of the majority of the cloud/aerosol contaminated bins, but it also causes a significant reduction in the number of valid profiles: only about 1% of the original data sample meets the filtering criteria. The effect of the different screening steps on the dataset regarding the number of Aeolus profiles is resumed in Table 2, where the procedure is applied to the Aeolus L1B dataset considered in this study.

4.2. In-water optical properties retrieval

The background-subtracted ground bin signal for the Aeolus Mie channel (S_{23}^{Mie}), generated by the interaction of the emitted laser radiation with two media (atmosphere and ocean) and their interface, can be expressed by the following equation:

$$S_{23}^{Mie} = E_0 A C_{instr} T_{A\_tot}^2 \bullet \left(\frac{B_{atm}}{(H + r1_{grd})^2} + \frac{B_{surf}}{(H + r2_{grd})^2} + \frac{\mu T_s^2 B_{wat}}{(n(H + r2_{grd}) + r3_{grd})^2} \right). \quad (1)$$

where:

- E_0: transmitted pulse energy;
- A: receiver area;
- C_{instr}: constant depending on the factors affecting the instrumental signal transmission;
- n: seawater real refractive index;
- H: range at the top of the ground bin;
- r_{1grd}, r_{2grd}, r_{3grd}: distance between the top of the bin and the half path of the atmospheric portion of the ground bin, the surface and the half path of the water sub-surface portion of the ground bin, respectively;
- T_A: transmission through the atmosphere;
- μ: $\cos(\theta_a)/\cos(\theta_w)$, where $\theta_a$and θ_w are the Aeolus slant angles off nadir in-air and in-water, respectively. This term accounts for the Straubel's invariant equation (please refer to section 13.1.2 in Mobley et al., 2021).
- T_S: transmission through the sea surface, down (↓) and up (↑), respectively.
- B_{atm}, B_{surf}, and B_{wat}: the volume scattering coefficients at a scattering angle of π radians for the back-scattering components from the atmosphere, the surface, and the water sub-surface, respectively. This latter term, which includes both extinction and back-scattering of all components, can be expressed as:

$$B_{wat} = \int_{r2_{grd}}^{r} \beta_{wat}(\pi, r') \bullet exp\left[-2 \int_{r2_{grd}}^{r'} K_{lid}(r'') dr'' \right] dr'; \quad (2)$$

where:

- $\beta_{wat}(\pi,r)$ is the in-water volume scattering coefficient at a scattering angle of π radians, which is the sum of the back-scatter from water molecules and suspended particles (β_{watM} and β_{watP}, respectively),

Table 2
List of the screening steps applied sequentially to the Aeolus L1B dataset, baseline B11, resolution measurement level. The number of profiles refers to the sum of Aeolus profiles selected after each step for the 7 ROIs from June 2020 to May 2021.

Filtering steps	*Number of profiles*
Starting data (10 km horizontal resolution)	2,800,000 (100%)
1) Dummy values	1,210,000 (43%)
2–4) Bathymetry, Shallow or deep-water ground bin and wind	350,000 (12%)
5) Low SNR values	250,000 (9%)
6–7) High SNR and Signal values	38,000 (~1%)

- K_{lid} is the already defined in-water lidar attenuation coefficient.

Eq. (1) is the starting point for the Aeolus ocean lidar algorithm. Neglecting the B_{surf} contribution (see Section 3), considering that $n(H + r2_{grd}) \gg r3_{grd}$ and assuming $r2_{grd} \approx r1_{grd}$:

$$S_{23}^{Mie} = \frac{E_0 A C_{instr}}{(H + r1_{grd})^2} \bullet T_{A_{tot}}^2 \bullet \left(B_{atm} + \frac{\mu T_s^2 B_{wat}}{n^2} \right) \quad (3)$$

To account for the instrument characteristics and the contribution due to the atmosphere in the signal acquired by bin 23, the information in bins 21 and 22 is also considered. Thus, the background subtracted and range corrected signal for Aeolus bins 21, 22, and 23 (S_{21}^*,S_{22}^* and S_{23}^*) can be described by the following equations:

$$S_{23}^* = M_{Mie} T_A^2 T_{21}^2 T_{22}^2 \left(B_{23} + \frac{\mu T_s^2 T_{23}^2 B_{wat}}{n^2} \right) \quad (4)$$

$$S_{22}^* = M_{Mie} T_A^2 T_{21}^2 B_{22} \quad (5)$$

$$S_{21}^* = M_{Mie} T_A^2 B_{21} \quad (6)$$

where:

- $T_{A\_tot} = T_A T_{21} T_{22}$
- B_{21}, B_{22} and $B_{23} = B_{atm}$ are the atmospheric back-scattering contributions for bins 21, 22 and 23, respectively. Each term consists of two distinct (aerosols and molecular) contributions: $B_x = B_{xa} + B_{xm}$
- T_A is the atmospheric transmission above bin 21
- T_{21}, T_{22} and T_{23} are transmission terms for bins 21, 22 and 23, respectively. These terms consist of two distinct (aerosols and molecular) contributions: $T_x = T_{xa}\, T_{xm}$
- T_S is the sea surface transmittance
- n is the effective refractive index of water; i.e., the refractive index value that describes the integral effect on the water column sensed by the bin
- M_{Mie} accounts for all terms in the complete signal equation due to the instrument

The following assumptions have been additionally adopted to reduce the number of unknowns:

- for the ground bin, the sea surface back-scattering and the ocean bottom contribution are negligible (please see Section 3).
- each bin is characterized by an effective back-scatter B_x and transmission T_x terms where the back-scattered signal is attenuated only by the bins above the bin generating the back-scattering. This is not valid for the ground bin, where the transmission term is applied only to the in-water contribution but not, for consistency with the other bins, to the atmospheric back-scattering of the bin itself.
- the sea surface transmittance T_S is assumed to be the same upward and downward and has a fixed value of 0.98 (Churnside, 2013).
- the refractive index is kept constant with a value equal to 1.356.
- back-scattering from marine particulate is assumed to be negligible with respect to that of pure sea-water ($\beta_{watM} > > \beta_{watP}$).

All steps to extract B_{wat} by combining Eqs. 4–6 are described in Appendix A, and only the final form of B_{wat} is given here:

In summary, Eq. (7) shows that it is possible to calculate analytically the term B_{wat}, which includes all in-water contributions to the signal (back-scattering and attenuation from all components), using the range-corrected signals of bins 21,22,23 (S_{21}^*, S_{22}^* and S_{23}^*) and the corresponding geometry (z_{21},z_{22} and z_{23}). To estimate the molecular scattering of bin 21 (B_{21m}) and the total molecular transmittance ($T_{BLm}^2 = T_{21m}^2 T_{22m}^2 T_{23m}^2$, respectively) the profile of atmospheric density ρ_j^m is computed starting from the pressure and temperature profiles provided by Aeolus AUX_MET files following Bodhaine et al., 1999. The atmosphere is assumed to be a pure scatterer (i.e., $\sigma_{ext}^m = \sigma_{sca}^m$). This implies neglecting atmospheric gases absorption that, for the wavelength of interest is mostly due to O_3 and NO_2. The hypothesis is that, in open sea, the concentration of tropospheric O_3 and NO_2, mostly due to anthropogenic activity is negligible. To estimate the aerosols transmittance term, the aerosol scale height has been fixed to $z_s = 1.5$ km (Qiu et al., 2005; Tsai et al., 2011). A sensitivity study (not shown) performed varying z_s between 1 and 2.5 km attested shows that the variation of this parameter has no significant impact on both the central value and the variability of the distribution of B_{wat} for all selected ROIs. All values with a percent relative error ($\Delta B_{wat} / B_{wat}$, see Section 5.3) larger than 100% are not processed in the successive processing steps.

Once estimated the overall water volume contribution (B_{wat}), the next step is to retrieve K_{lid} of Eq. (2). Having a single piece of information, the contribution from pure sea water and chlorophyll is estimated through ancillary information (see Section 2.3). This is practically implemented applying the 3-D LUT described in Section 3.

Specifically, the input values used for the LUT are:

- *Chl-a* concentration derived by daily ESA-0C-CCIv6 multisensor products (see Section 2.3);
- P_n^w parameter: the radiant power ratio due to the water column, where $P_n^w = B_{wat} \bullet \Delta\Omega_r$ and $\Delta\Omega_r$ is the in-water solid angle of the receiver estimated using the information associated to each measurement.

A 2-D linear interpolation is then combined with the LUT to produce interpolated values $K_{\mathrm{lid}} = LUT(Chla, P_n^w)$.

The estimation of K_{lid} using the LUT necessitates that the input variables Chl-a and P_n^w meet the following temporal (±24 h) and spatial (<±20 km) matching criteria.

5. Results

The validation of the estimated Aeolus-OC variables (B_{wat} and K_{lid}) is described and discussed here. Table 3 reports seasonally, for each ROI, the number of B_{wat} and K_{lid} values that passed the Q/C and data screening procedure developed, respectively. Seasonal differences are expected primarily due to cloud cover seasonal cycle and aerosol variability. The number of valid K_{lid} estimation is further reduced with respect to B_{wat} because of the availability of Chlorophyll-a concentration derived by passive satellite remote sensors and used as ancillary data. Due to the relatively small dimensions of the datasets, in particular for K_{lid} values, the seasonal analyses were not performed as not statistically significant.

Two reference datasets are used for two different validation approaches:

$$B_{wat} \approx \frac{(S_{23}^* - S_{22}^*)}{S_{21}^*} \frac{B_{21m} n^2}{T_s^2 T_{BLm}^2} \frac{1}{T_{BLa}^2} \approx \frac{(S_{23}^* - S_{22}^*)}{S_{21}^*} \frac{B_{21m} n^2}{T_s^2 T_{BLm}^2} e^{+\left(\left(-ln\left(\frac{B_{21m}}{B_{22m}} \frac{1}{T_{21m}^2} \frac{S_{22}^*}{S_{21}^*} \right)^{\frac{e^{\frac{z_{21}}{z_s}}}{\Delta z_{21}}} \right) \left(e^{\frac{-z_{21}}{z_s}} \Delta z_{21} + e^{\frac{-z_{22}}{z_s}} \Delta z_{22} + e^{\frac{-z_{23}}{z_s}} \Delta z_{23} \right) \right)}. \quad (7)$$

Table 3
Number of valid Aeolus-derived B_{wat} and K_{lid} estimations.

Region\Season	DJF		MAM		JJA		SON		ALL	
	B_{wat}	K_{lid}	B_{wat}	K_{lid}	B_{wat}	K_{lid}	B_{wat}	K_{lid}	B_{wat}	K_{lid}
NASTG	544	193	441	146	291	127	487	252	1763	718
SASTG	350	212	263	130	241	140	113	79	967	561
NWMED	10	8	6	4	52	44	27	17	95	73
SEMED	51	34	55	40	170	144	89	64	365	282
NASPG	4	0	19	0	26	3	23	1	72	4
BLSEA	4	1	6	4	32	22	14	10	56	37
SOIND	43	24	27	9	58	3	27	19	155	55

- statistical validation using BGC-Argo dataset of the diffuse attenuation coefficient, K_d at 380 nm (Section 2.2);
- match-up validation using a_{cdm} at 412 nm from ESA-OC-CCI dataset (Section 2.3).

5.1. Statistical validation

Creating a classic coincident and collocated dataset between Aeolus and BGC-Argo floats results in a limited amount of valid match-ups (Loew et al., 2017). Thus, in order to exploit the information provided by BGC-Argo, a statistical approach is applied to compare in-situ and Aeolus-derived statistical properties at a regional level. The statistics are derived from temporally extended (~10 years) BGC-Argo measurements (see Table 1) and from spatially extended Aeolus retrieved variables (Table 3) within each ROI.

A qualitative comparison is performed, without any homogenization of the used datasets, between the cumulative histograms of Aeolus-OC products B_{wat} and K_{lid} at 355 nm and K_d at 380 nm obtained by BGC-Argo measurements. These curves are depicted in Fig. 8, where different colors are used for each ROI.

The results confirm the expected regional pattern between the compared variables: an inverse relationship characterizes K_d and B_{wat} and a direct one for K_d and K_{lid}. The rationale to perform this comparison also for an intermediate variable, such as B_{wat}, is because of the further reduction (50%) of the Aeolus database when retrieving K_{lid} due to the availability of Chl-a ancillary data within the fixed matching criteria (see Section 4.2).

5.2. Match-up validation

An additional exercise to validate K_{lid} has been performed using the a_{cdm} product at 412 nm released by ESA-OC-CCI. This approach allows for generating a statistically significant match-up dataset. On the other hand, a_{cdm}, besides the fact that is derived from an assumed relationship with chlorophyll, also needs to be homogenized in terms of variable definition and spectral dependence.

Specifically, a_{cdm} is the sum of CDOM and Non-Algal Particles (NAP) absorption contributions (a_{CDOM} and a_{NAP}, respectively), but in the UV and in the open ocean and for various trophic conditions, the a_{cdm} can be assumed to be dominated by a_{CDOM} (Bricaud et al., 2010; Morel et al., 2007; Siegel and Michaels, 1996; Smyth, 2011). In parallel, the retrieved K_{lid} can be decomposed to compute the Δa budget that does not depend on the absorption of pure seawater and of the pigmented and not-pigmented particulate matter ($a_{wat_mol}$and a_p, respectively):

$$\Delta a(355) = K_{lid}(355) - a_{wat\_mol}(355) - a_p(355),$$

where $a_{wat\_mol}(355)$=0.00097 for pure seawater with $T = 16$ °C and S = 35.5 PSU (Röttgers et al., 2016). According to Mobley et al. (2021), $a_p$can be estimated as $a_p = 0.052 \bullet Chl - a^{0.635}$.

The term $\Delta a(355)$ can also be written as:

$$\Delta a(355) = a_{CDOM}(355) + a_{NAP}(355). \quad (8)$$

Eq. (8) shows that the Δa parameter retrieved by Aeolus is, theoretically, comparable with a_{cdm} derived at $\lambda = 412$ nm by satellite standard ocean color passive measurements. Furthermore, this approach scheme avoids the necessity to use specific functional relationships between a_{CDOM} and $Chl - a$ concentration. To take into account the different wavelengths between Δa and a_{cdm} products (i.e. 355 vs. 412 nm), assuming that a_{NAP} can be neglected, several spectral models can be adopted (e.g., Pitarch, 2017; Mobley et al., 2021; Terzić et al., 2021). It is important to recall that current spectral models are based on specific experimental studies that may lack representativeness due to the unavailability of global ocean color measurements at these wavelengths (i.e., UV). In our case, the model suggested by Pitarch (2017) is used:

$$a_{CDOM}(355) = a_{cdm}(412) \bullet exp[-0.014(355-412)]. \quad (9)$$

Then, to compare Aeolus and ESA-OC-CCI measurements, the following match-up criteria were adopted:

- Temporal matching: to increase the number of match-ups, the temporal difference between Aeolus and ESA-OC-CCI is ±24 h (i.e., if there is no match-up for the day of the Aeolus measurements, the match-up is searched in the previous or the next day).
- Spatial matching: a square of 5 × 5 pixels of ESA-OC-CCI a_{cdm} product, corresponding to about 20 × 20 km, is selected around the Aeolus lat-lon measurement.
- Number of valid pixels (i.e. pixels that are not flagged for the presence of disturbing effects that compromise OC measurements such as aerosols, clouds, sunlight, etc.…): to achieve the best possible number of match-ups, the number of valid pixels is kept very low. If there are at least 16% of valid pixels, a_{cdm} is calculated as the mean value of these pixels.

Fig. 9 shows the scatter plot between the median values calculated for the different 7 ROIs for the a_{cdm} product released by ESA-OC-CCI at 412 nm and scaled at 355 nm and the Δa at 355 nm retrieved by Aeolus measurements. As already mentioned, one year of the Aeolus dataset has been considered for this comparison, and only Aeolus data with the relative uncertainty $\Delta B_w/B_w \leq 1$ (see Section 5.3) is considered. Horizontal (vertical) lines refer to the interquartile range of ESA-OC-CCI (Aeolus) datasets. The choice of relying on the median and the percentile values is taken to reduce the effect of the high noise affecting single match-ups. A quite good agreement between the two compared variables emerges from Fig. 9: the oligotrophic regions in the Atlantic Ocean (SASTG and NASTG), which have a statistically significant number of match-up pairs, exhibit similar values of Δa and a_{cdm} as well as SOIND and NWMED regions, for which a lower number of match-up, but still significant, was found.

For the SEMED region, the median value of Δa is higher than the one retrieved for NWMED. This result could be explained by the fact that, for both regions, >50% of the values refer to the June–July-August (JJA) period (see Table 3) where, on one side, oligotrophic conditions characterized similarly both seas but, on the other, the presence of not flagged aerosol dust in the Aeolus bin 23 near the surface could differently affect the retrieved value of Δa in these two regions. A disagreement between Δa and a_{cdm} values characterizes the BLSEA region. This result could be due to the different trophic regimes of this region, as

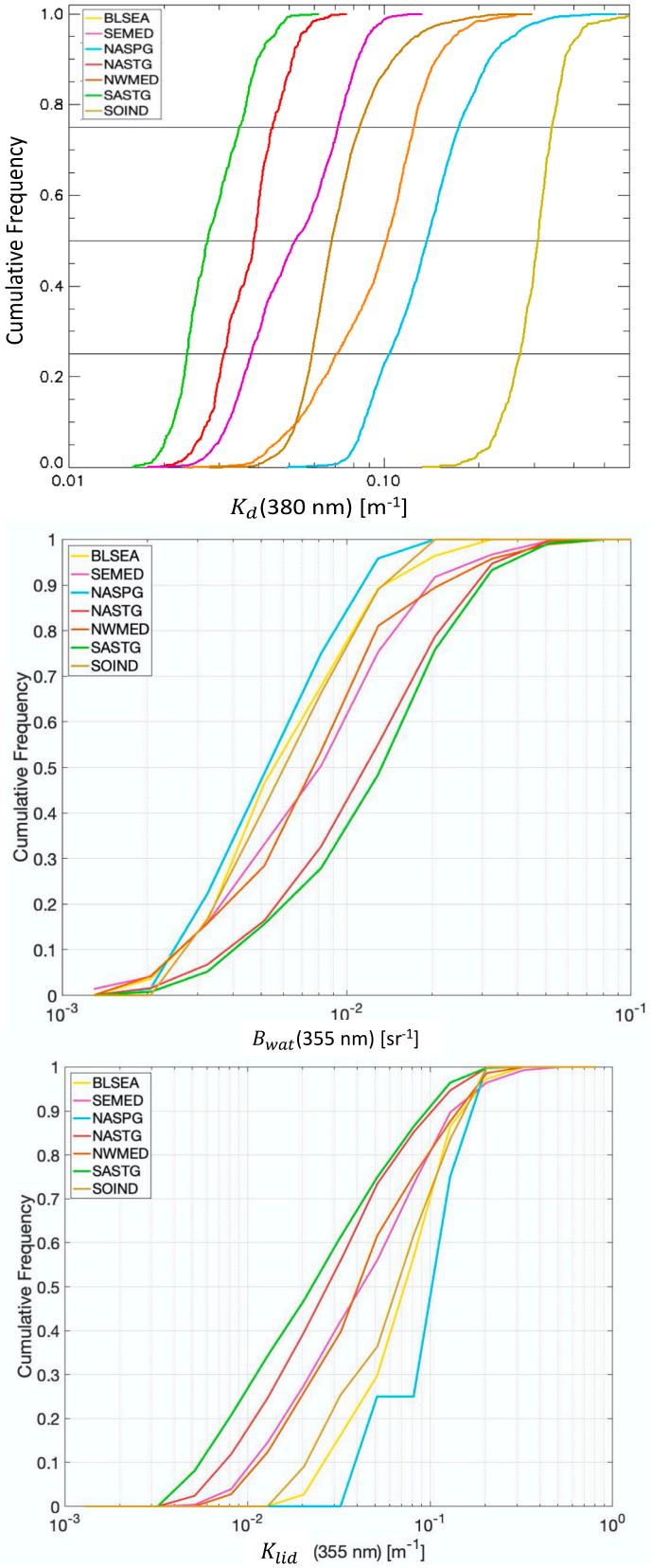

Fig. 8. Cumulative frequency distribution of: a) K_d at 380 nm for all BGC-Argo subsets (upper panel); b) Aeolus derived B_{water} at 355 nm (middle panel); c) Aeolus derived K_{lid} at 355 nm (lower panel). Different colors are used for each ROI.

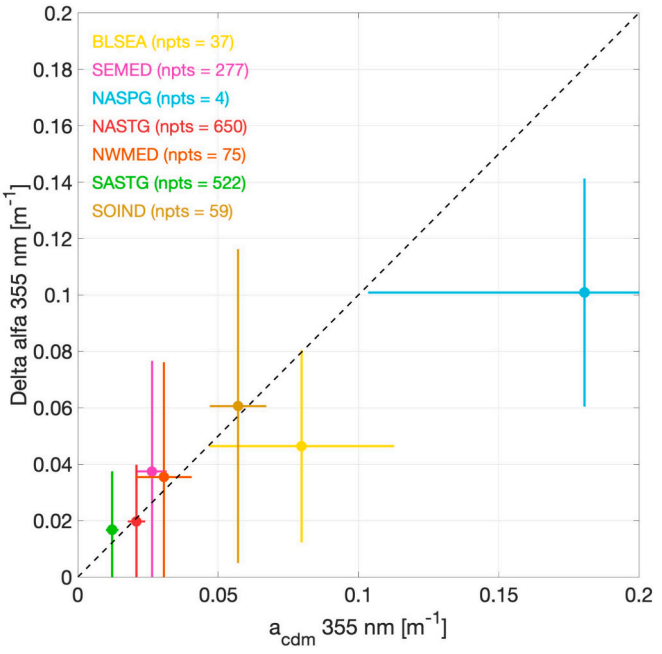

Fig. 9. Scatter plot between the median values of a_{cdm} product released by ESA-OC-CCI and the Δa parameter retrieved by Aeolus calculated for the 7 ROIs from June 2020 to May 2021. Horizontal (vertical) lines refer to the interquartile range of ESA-OC-CCI (Aeolus) datasets.

highlighted by BGC-Argo statistical analyses (not shown), but the low number of valid match-ups prevents any further analysis. Finally, the results on the NASPG region are not statistically significant due to the low number of match-ups.

In summary, for the ROIs with a significant number of match-ups (i.e. SASTG, NASTG, SEMED, NWMED and SOIND), the agreement found between Δa and a_{cdm}, although depending on several assumptions, demonstrates that the developed Aeolus-OC algorithm can estimate, at a global scale, a geophysical variable that gives information about the ocean's optical state. These ROIs, excluding SOIND, exhibit low values in terms of Δa and a_{cdm} that are characteristics of oligotrophic conditions. On the contrary, the ROIs with high values of Δa and a_{cdm} (i.e. BLSEA, NASPG) are characterized by a small number of match-ups which undermines the robustness of the results of this validation. Furthermore, Fig. 9 also highlights that, for the above mentioned ROIs with a statistically significant number of match-ups, the interquartile ranges of Δa may be one order of magnitudes higher than those computed for a_{cdm}. This attests that, at regional scale, the high variability affecting single match-ups does not allow to deduce any relevant relationships between Δa and a_{cdm}.

5.3. Analysis of uncertainties

The identified sources of uncertainty to be considered in the overall uncertainty budget originate from the structure of the retrieval algorithm:

1) Screening procedure: the flagging process introduces uncertainties due to the developed methodology and the adopted thresholds;
2) B_{wat} estimation: this phase is based on analytical retrieval that makes use of assumptions (e.g., on the aerosol optical properties);
3) K_{lid} estimation: this final phase introduces sources of uncertainties associated to the generation of the LUT, the LUT inputs, and the adopted interpolation scheme.

Providing a complete, quantitative and detailed uncertainty budget requires not only the characterization of each single input source but also the development of methodologies to quantify uncertainties associated to the non-analytical steps of the retrieval (e.g., threshold based flagging). In addition, estimating the uncertainties introduced by the adopted assumptions may be complex. As an example, to investigate the impact on B_{wat} due to the assumption (Section 4.2) of a constant aerosol scale height (z_s) value in the lowermost 3 atmospheric bins (21, 22 and 23), a sensitivity study was performed varying z_s between 1 and 2.5 km (Qiu et al., 2005). The variation of this parameter resulted to have relatively low impact (<10%) on the distribution properties (median and interquartile range) of the retrieved B_{wat} values for all selected ROIs. However, this exercise does not really evaluate the uncertainty due to the assumption but only the sensitivity to the value used in the assumed scenario.

For the above reasons, in this study, we focus on the expected primary source of uncertainty associated to the Aeolus measurement: the radiometric noise. Neglecting its impact in the screening phase of the algorithm, radiometric noise's uncertainty contribution in the second step of the retrieval is estimated by applying the error propagation formula to the analytical solution used for the retrieval of B_{wat} (see Appendix B for further details) to each single retrieved value.

Fig. 10 shows the scatter plots, for each ROI, of the estimated relative uncertainty (i.e. $(\Delta B_{wat}/B_{wat})$x100) as a function of the retrieved B_{wat} parameter. This figure shows that, approximately below $B_{wat} = 0.005$ (sr^{-1}), the relative radiometric error is equal to or higher than 50%. It also emerges that based on the combination of SNR constraints ($SNR_{low} < SNR < SNR_{high}$) and the fact that the current retrieval uses data from 3 bins (see Sections 4.1 and 4.2, respectively), it is reasonable to expect a minimum relative error in the order of 30%.

In principle, the total uncertainty introduced by the last step of the inversion algorithm (see Section 4.2) should account for contributions due to:

- the accuracy of the radiative transfer model;
- the uncertainty associated to the values of the variables (*Chl-a* and P_n^w) used as input of the LUT;
- the uncertainty due to the interpolation to obtain the final K_{lid} value.

We focus again on the expected largest sources of uncertainty that, in this processing step, are the LUT input values (*Chl-a* and P_n^w) assuming as negligible the other sources. A sensitivity analysis was performed by perturbing statistically the LUT input values on the basis of their associated uncertainties. A median value of the absolute percent difference of K_{lid} from unperturbed and uperturbed inputs, is of the order of 50%. However, the average value is larger (80%) because of the skewed distribution of the results.

It should be noted that, as expected, because of the relatively low absorption form Chl-a at 355 nm, the uncertainty on the retrieved K_{lid} is mostly driven by the quality of P_n^w. This implies that to improve the accuracy of the estimated K_{lid} requires a reduction of radiometric noise. This can be partially obtained by adopting a different cloud screening algorithm that does not remove all observations with relatively high SNR, as well as, trying to implement a processing that integrate spatially the single measurement signals.

Having considered, in the above described uncertainty estimation process, only the radiometric noise, this result is clearly an underestimation of the genuine uncertainty.

6. Conclusions

The ALADIN lidar instrument onboard the Aeolus satellite has been the first HSRL UV Doppler lidar deployed in space. Although designed to provide atmospheric wind profiles for the improvement of numerical weather forecasting (Rennie et al., 2021), the unprecedented types of measurements from this mission are expected to contain crucial and

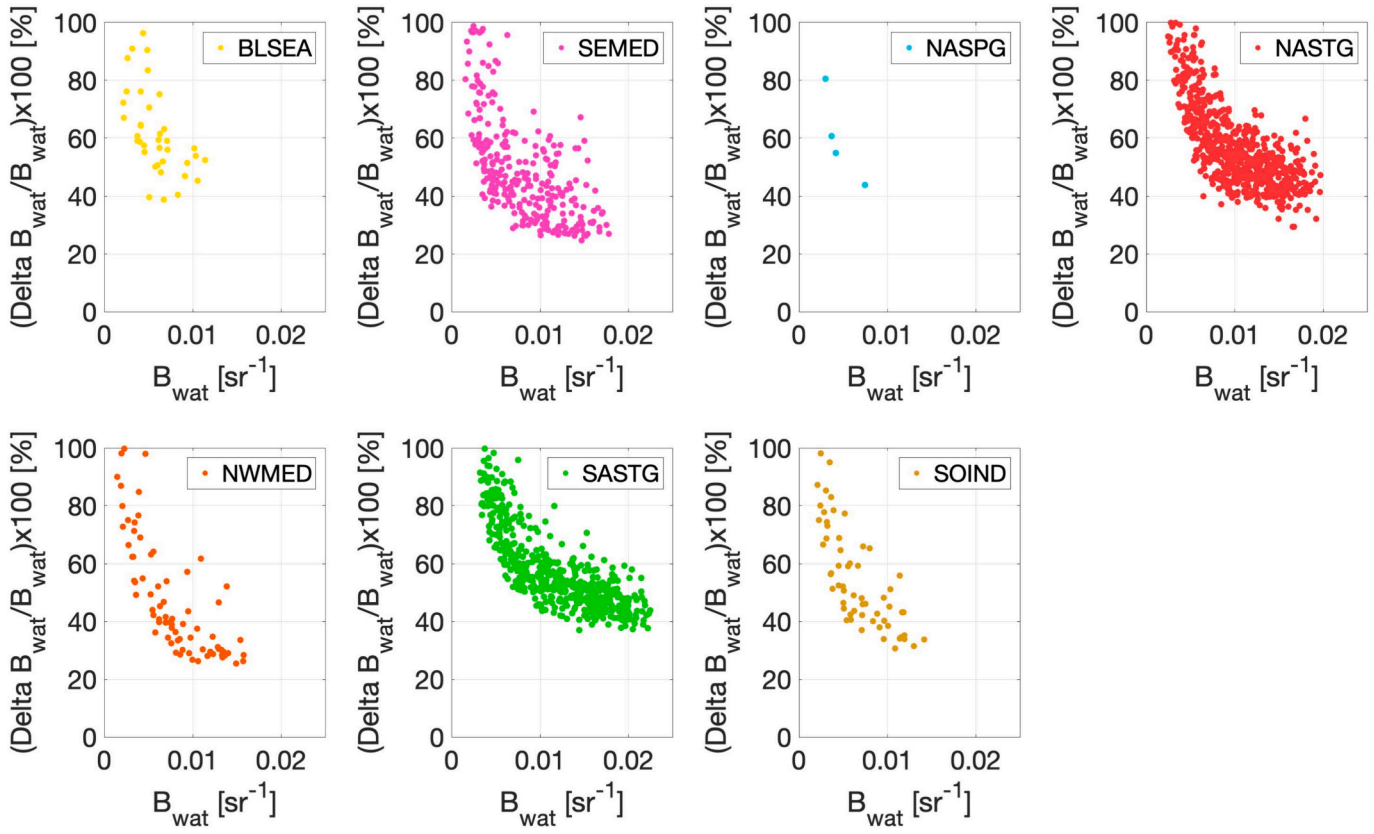

Fig. 10. B_{wat} relative uncertainty (%) due to signal noise as a function of B_{wat} for different ROIs.

unique information regarding the potential application to retrieve optical properties of the observed ocean volume.

The objective of this study is to evaluate the feasibility of deriving ocean optical properties using Aeolus measurements.

This has been accomplished by performing two parallel and interacting research activities. On one hand, the quantitative interpretation of Aladin observations, as well as the sensitivity of the collected signal to different variables, required a numerical model to simulate the signal for different geophysical scenarios. On the other hand, the statistical analyses of Aladin observations permitted to develop criteria to screen out the data that could not be used in the current retrieval algorithm.

The Aeolus data analysis and the results of LiOC simulations allowed the design of a filtering data procedure that removes most of the low-quality and cloud/aerosol-contaminated Aeolus bins filtering out about 99% of the dataset.

After filtering out undesired observations, a two-step procedure, designed using only the signal acquired by the Aeolus Mie channel, is applied to estimate two parameters:

- B_{wat}: the in-water contributions to the signal retrieved through the EBL approach. This parameter is obtained by solving analytically a system of signal equations for bins 21, 22 and 23 of the Aeolus Mie channel coupled with assumptions on the molecular and aerosol properties of the Marine Atmospheric Boundary Layer and on the sea-surface contribution.
- K_{lid}: the in-water lidar attenuation term. This retrieval relies on 3D LiOC-derived LUTs that use as input the estimated B_{wat} and the Chl-a concentrations from ancillary satellite measurements as input values.

It is important to highlight that B_{wat} and K_{lid} represent the first OC-related products derived by a space-borne lidar mission in a spectral region (355 nm) not covered by operational OC products.

The validation of these products consisted in comparing 1-year of Aeolos quality controlled dataset, over a set of oceanic regions representing different global scenarios, against:

1) BGC-Argo measurements. The statistical comparison between the Aeolus-OC derived values B_{wat} and K_{lid} at 355 nm with BGC-Argo values of K_d at 380 nm demonstrates the sensitivity of the Aeolus measurements to marine optical properties. These findings attest a general accordance between OC reference measurements and the proposed Aeolus-OC products.
2) ESA-OC-CCI dataset. The match-up comparison in terms of median values at a global scale between the Δa parameter retrieved by Aeolus and a_{cdm} derived by satellite standard ocean color passive measurements shows that CDOM measurements can be derived by Aeolus measurements. However, the reduced number of valid Aeolus OC products for BLSEA and NASPG ROIs limits the robustness of the validation results only to oligotrophic water regions. Furthermore, the high variability affecting single match-ups undermines the possibility of conducting this comparison on a regional scale.

Both validation exercises confirmed the sensitivity of the measurement to the estimated variables as well as an overall agreement. As mentioned, major issues arise in using the Aeolus signal in ocean regions characterized by complex water regimes because, in such highly absorbing regimes the backscattered signal is weak, and hence the sensitivity to radiometric noise becomes relevant. The classical match-up suffers from a low number of valid points due mainly to the lack of AEOLUS data meeting the OC quality requirements. To increase this number, in the future, a possible strategy is enlarging the size of Aeolus dataset extending the considered temporal series over well characterized ROIs. This implies the use of homogenous and quality checked measurements.

The main limitation of the proposed products derives from the fact that the primary objective of the Aeolus mission is to acquire profiles of Earth's wind. Consequently, system design, acquisition characteristics, and data processing are optimized for this application. This configuration implies that the instrument's potential to sense marine optical properties cannot be thoroughly investigated Furthermore, the information content residing in the HSRL capabilities has not been exploited due to the lack of characterization of the instrument for the marine environment. Moreover, the Aeolus vertical sampling protocol does not allow to exploit the lidar profiling capabilities in the ocean.

Another constraint of the proposed products is the assumptions made to account for the contribution of atmospheric aerosols in the ground-bin signal. These assumptions (e.g., simplified vertical distribution) are adopted because of a lack of information regarding aerosol properties in the Aeolus ground bin. In fact, retrieved extinction coefficients through the standard correct algorithm (SCA) developed for the Aeolus aerosol product (L2A, Flament et al., 2021) are characterized by a significant bias below 2 km (Ehlers et al., 2022). Furthermore, this product is available at coarse horizontal scales of 87 km, whereas, in this study, Aeolus measurement resolution dataset is considered (3 km horizontal resolution). Moreover, the characterization of the ground bin in terms of aerosol properties is not the primary objective of this project.

Having demonstrated the sensitivity to the marine optical properties and the capabilities to recognize different regimes, the uncertainties associated to the prototype products are estimated. The primary source of uncertainty is the radiometric noise, and on this basis, the uncertainty associated with the prototype product is estimated accounting only for this contribution. This estimation does not include the uncertainty introduced by the flagging process and by the assumptions made to derive B_{wat}. In this context, the potential integration of ancillary information on the optical properties of aerosols and, in particular, their height dependence, could reduce the impact of the aerosol uncertainty. Other significant sources of uncertainty derive from geophysical disturbances, such as the presence of clouds along the sensed path, as well as the contribution of aerosols, in terms of back-scattering/extinction, to the measured signal. Additional uncertainties, such as assumptions related to the analytical model, including the impact of surface wind and the uncertainties inherent in the entire forward modeling process and its outputs, have a secondary-level influence.

7. Perspectives

In summary, this study has shown how the recently decommissioned ALADIN ADM-Aeolus mission offered an opportunity to investigate space-borne lidar potentials for oceanic applications. This mission was specifically designed for wind profile retrieval in the atmosphere, which imposes spatial resolution limits for marine applications. Despite the relatively short lifetime of the ALADIN ADM-Aeolus mission, the limited spatial sampling, the coarse vertical resolution, and some issues about the homogeneities of observations during the mission operations, this study was able to provide statistical evidence of the sensitivity to the CDOM variability on a temporal/seasonal and spatial/regional basis.

In the future, some specific retrievals could be employed to integrate into the OC Aeolus developed algorithm the ancillary information on the optical properties of aerosols. One potential approach is using the recent version of the Profile Processor algorithm (AEL-PRO) developed for Aeolus (Donovan et al., 2021). This product could be applied to estimate the aerosol total transmittance term T^2_{BLa} (see Eq. 7), overcoming the assumptions adopted to describe the vertical distribution of the aerosols in the lowermost 3 atmospheric bins (see Section 4.2 and Appendix A). Similarly, this approach should also provide an expected improvement in cloud detection.

Some of the ALADIN ADM-Aeolus limits could be partially overcome by Aeolus-2, which is expected to rely on a laser source with an average power three to four times higher than the onboard Aeolus, with a consequent increase (up to twofold) in measurement precision. Noteworthy is that the capability to meet operational requirements can benefit from the lidar optimization by trading between precision and horizontal resolution (i.e., the possibility to increase the SNR based on a partial degradation of the horizontal resolution or, conversely, to increase the spatial resolution based on a degradation of the precision).

The tools developed for this study may be adapted to planned/future space lidar missions. In this context, the characteristics of ATLID lidar onboard of EarthCARE mission (Illingworth et al., 2015), launched in May 2024, could improve both cloud detection and optical characterization of atmospheric and oceanic particles in the proposed retrieval. Specifically, the ATLID polarization capability will improve the detection of the detection of atmospheric aerosol and clouds and the characterization of oceanic particles by integrating the OC algorithm used for CALIOP data (Behrenfeld et al., 2013; Lu et al., 2021) in the proposed retrieval. Furthermore, the higher vertical resolution of ATLID measurements allow better discriminating the different signal contributions (i.e. atmosphere, sea-surface, in water) acquired in the ground bin (see Section 4.2). In addition, the information derived by the other instruments onboard, will improve the characterization of the observed scene in terms of the presence of cloud and aerosol. Finally, the limitations identified in the current study in terms of vertical resolutions and estimation of the ocean optical properties estimation in the UV range could be overcome by the future Cloud Aerosol Lidar for Global Observations of the Ocean–Land–Atmosphere (CALIGOLA) mission (Behrenfeld et al., 2023; Di Girolamo et al., 2024). This mission is being conceived for interdisciplinary purposes, aiming at remote sensing tasks in both the atmosphere and the ocean. In particular, the planned ocean capabilities will allow for the independent retrieval of ocean attenuation and backscattering profiles at 355 and 532 nm and the integrated-column chlorophyll fluorescent signal at 680 nm. This design will enable significant advances for the ocean science community.

Description of author's responsibilities

The general conception of this work was developed by DD and GLL. DD, GLL, DAD and MDP implemented and refined the Aeolus retrieval procedure for ocean. DD performed most of the AEOLUS data analysis with contributions from MDP, GGL, DAD and advice from all co-authors. EO performed the analysis of the BGC-Argo measurements, whereas SC analysed ESA-OC-CCI dataset. All co-authors contributed to the interpretation of the results. DD wrote the paper with input from GLL, DAD and MDP. All co-authors provided critical comments to the manuscript.

CRediT authorship contribution statement

Simone Bucci: Software, Data curation, Writing – review & editing. **Claudia Cesarini:** Project administration, Writing – review & editing. **Simone Colella:** Validation, Software, Data curation, Writing – review & editing. **Davide D'Alimonte**: Software, Methodology, Investigation, Formal Analysis, Writing - review & editing. **Lorenzo Di Ciolo:** Data curation. **Paolo Di Girolamo:** Visualization, Writing – review & editing. **Marco Di Paolantonio:** Software, Methodology, Investigation, Formal analysis, Writing – review & editing. **Noemi Franco:** Data curation, Writing – review & editing. **Giacomo Gostinicchi:** Data curation, Writing – review & editing. **Giovanni Giuliano:** Data curation, Writing – review & editing. **Tamito Kajiyama:** Software, Data curation, Writing – review & editing. **Emanuele Organelli:** Software, Data curation, Writing – review & editing. **Rosalia Santoleri:** Conceptualization, Writing – review & editing. **Gian Luigi Liberti:** Visualization, Validation, Software, Methodology, Formal analysis, Conceptualization, Writing – review & editing. **Davide Dionisi:** Visualization, Validation, Supervision, Software, Resources, Project administration, Methodology, Investigation, Funding acquisition, Formal analysis, Data curation, Conceptualization, Writing - review & editing, Writing - original draft.

Declaration of competing interest

The authors declare the following financial interests/personal relationships which may be considered as potential competing interests:

Davide Dionisi reports financial support was provided by European Space Agency. If there are other authors, they declare that they have no known competing financial interests or personal relationships that could have appeared to influence the work reported in this paper.

Data availability

Data will be made available on request.

Acknowledgements

All AEOLUS data used are owned by ESA (European Space Agency) and made publicly accessible.

The Argo Program is part of the Global Ocean Observing System (GOOS). BGC-Argo data were collected and made freely available at the Coriolis database at ftp://ftp.ifremer.fr/ifremer/argo (Argo float data and metadata from Global Data Assembly Centre (Argo GDAC), 2023).

ESA supported this study as part of the Aeolus+Innovation program (contract No. 4000133933/21/I-BG) within the "CDOM-proxy retrievals from aeOLus ObseRvations" project (COLOR, http://ricerca.ismar.cnr.it/color/). The authors acknowledge the helpful inputs and advices by Marie-Helene Rio of ESRIN-ESA during the COLOR project execution.

Appendix A (B_{wat} retreval)

Starting from Eq. (4-6) described in Section 4.2, the objective is to extract the water contribution term B_{wat} from the ground bin measurement S^*_{23}. To reach this objective, it is necessary to estimate both the term M_{Mie} accounting for instrument characteristics as well as the atmospheric contributions.

To estimate the atmospheric contribution in S^*_{23}, the difference between S^*_{23} and S^*_{22} is computed:

$$S^*_{23} - S^*_{22} = M_{Mie} T^2_A T^2_{21} \left(\frac{\mu}{n^2} B_{wat} T^2_s T^2_{22} T^2_{23} + \left(B_{23} T^2_{22} - B_{22} \right) \right)$$

Separating the molecular and the aerosols contribution in the extinction and back-scattering terms, Eq. (A.1) can be rewritten as:

$$S^*_{23} - S^*_{22} = M_{Mie} T^2_{Aa} T^2_{21a} T^2_{Am} T^2_{21m} \left(\frac{\mu}{n^2} B_{wat} T^2_s \, T^2_{22a} T^2_{22m} T^2_{23a} T^2_{23m} + \left((B_{23a} + B_{23m}) T^2_{22a} T^2_{22m} - (B_{22a} + B_{22m}) \right) \right)$$

Assuming that the difference between atmospheric back-scattering contribution of bin 22 and 23 is negligible compared to the contribution of sea water, namely:

$$\frac{\mu}{n^2} B_{wat} T^2_s \, T^2_{22a} T^2_{22m} T^2_{23a} T^2_{23m} \gg (B_{23a} + B_{23m}) T^2_{22a} T^2_{22m} - (B_{22a} + B_{22m})$$

it is possible to obtain, from the difference $S^*_{23} - S^*_{22}$, the contribution from the sea with the transmission of the surface and the whole atmosphere:

$$S^*_{23} - S^*_{22} \approx M_{Mie} T^2_{Aa} T^2_{21a} T^2_{Am} T^2_{21m} \frac{\mu}{n^2} B_{wat} T^2_s \, T^2_{22a} T^2_{23a} T^2_{22m} T^2_{23m}$$

Eq. (A.3) can then be divided by S^*_{21}:

$$\frac{(S^*_{23} - S^*_{22})}{S^*_{21}} \approx \frac{1}{(B_{21a} + B_{21m})} \frac{\mu}{n^2} B_{wat} T^2_s \, T^2_{21a} T^2_{22a} T^2_{23a} T^2_{21m} T^2_{22m} T^2_{23m}.$$

In this way, the terms regarding the instrument parameters M_{Mie} and the atmospheric transmission above bin 21 are removed. Eq. (A.4) can be rewritten as:

$$\frac{(S^*_{23} - S^*_{22})}{S^*_{21}} \frac{n^2}{\mu T^2_s T^2_{21m} T^2_{22m} T^2_{23m}} \approx \frac{1}{(B_{21a} + B_{21m})} B_{wat} \, T^2_{21a} T^2_{22a} T^2_{23a}$$

Let us define the total transmittance T_{BLx} from surface to top of bin 21:

$$T^2_{BLx} = T^2_{21x} T^2_{22x} T^2_{23x}.$$

where $x = m$ or a, then:

$$\frac{(S^*_{23} - S^*_{22})}{S^*_{21}} \frac{n^2}{\mu T^2_s T^2_{BLm}} \approx \frac{1}{(B_{21a} + B_{21m})} B_{wat} \, T^2_{BLa}.$$

Assuming that, at 355 nm, the back-scattering is dominated by molecular contribution: $B_{21m} \gg B_{21a}$,

$$\frac{(S^*_{23} - S^*_{22})}{S^*_{21}} \frac{B_{21m} n^2}{\mu T^2_s T^2_{BLm}} \approx B_{wat} \, T^2_{BLa}.$$

In Eq. (A.8) all terms on the left side are known or can be estimated. We still have 2 unknowns on the right side T_{BLa} and B_{wat}.

The term of T^2_{BLa} can be retrieved by using the ratio of the range corrected signal of bin 21 and 22:

$$\frac{S^*_{22}}{S^*_{21}} = \frac{(B_{22a} + B_{22m})}{(B_{21a} + B_{21m})} T^2_{21a} T^2_{21m},$$

Assuming $B_{21m} \gg B_{21a}$ and $B_{22m} \gg B_{22a}$ (i.e. extending the assumption of dominant molecular back-scattering to the bin 21 and 22):

$$T_{21a}^2 = \frac{B_{21m} + B_{21a}}{B_{22m} + B_{22a}} \frac{1}{T_{21m}^2} \frac{S_{22}^*}{S_{21}^*} \approx \frac{B_{21m}}{B_{22m}} \frac{1}{T_{21m}^2} \frac{S_{22}^*}{S_{21}^*}.$$

The following assumptions on aerosol properties are, then, made:

- homogeneity of the aerosol type in the marine boundary layer
- known vertical distribution, for example:

$$T_{Xa}^2 = exp\left(-2\left(\frac{\rho_0 \sigma_{ext} \, e^{\frac{-z_X}{z_s}} \Delta z_X}{cos\theta} \right) \right).$$

Applying Eq. (A.11) to bin 21:

$$ln\left(T_{21a}^2\right) = -2\left(\frac{\rho_0 \sigma_{ext} \, e^{\frac{-z_{21}}{z_s}} \Delta z_{21}}{cos\theta} \right)$$

It is noteworthy that, having neglected the aerosol back-scattering, there is no need to make any assumption on the aerosol type. The term $\frac{2\rho_0 \sigma_{ext}}{cos\theta}$ can be retrieved combining Eq. (A.10) and Eq. (A.12):

$$\frac{2\rho_0 \sigma_{ext}}{cos\theta} = -\frac{ln\left(T_{21a}^2\right)}{\Delta z_{21}} e^{\frac{z_{21}}{z_s}} \approx -ln\left(\frac{B_{21m}}{B_{22m}} \frac{1}{T_{21m}^2} \frac{S_{22}^*}{S_{21}^*} \right) \frac{e^{\frac{z_{21}}{z_s}}}{\Delta z_{21}},$$

The aerosol transmittance from surface to top of bin 21 is:

$$T_{BLa}^2 = T_{21a}^2 T_{22a}^2 T_{23a}^2 = exp - \left(\frac{2\rho_0 \sigma_{ext}}{cos\theta} \left(e^{\frac{-z_{21}}{z_s}} \Delta z_{21} + e^{\frac{-z_{22}}{z_s}} \Delta z_{22} + e^{\frac{-z_{23}}{z_s}} \Delta z_{23} \right) \right),$$

Then, combining Eq. (A.8), Eq. (A.13), and Eq. (A.14):

$$B_{wat} \approx \frac{\left(S_{23}^* - S_{22}^*\right)}{S_{21}^*} \frac{B_{21m} n^2}{\mu T_s^2 T_{BLm}^2} \frac{1}{T_{BLa}^2} \approx \frac{\left(S_{23}^* - S_{22}^*\right)}{S_{21}^*} \frac{B_{21m} n^2}{\mu T_s^2 T_{BLm}^2} e^{+\left(\frac{2\rho_0 \sigma_{ext}}{cos\theta} \left(e^{\frac{-z_{21}}{z_s}} \Delta z_{21} + e^{\frac{-z_{22}}{z_s}} \Delta z_{22} + e^{\frac{-z_{23}}{z_s}} \Delta z_{23} \right) \right)},$$

In case of homogeneous vertical distribution in the MABL ($z_s = \infty$):

$$B_{wat} \approx \frac{\left(S_{23}^* - S_{22}^*\right)}{S_{21}^*} \frac{B_{21m} n^2}{\mu T_s^2 T_{BLm}^2} \left(\frac{B_{21m}}{B_{22m}} \frac{1}{T_{21m}^2} \frac{S_{22}^*}{S_{21}^*} \right)^{-\frac{\Delta z_{BL}}{\Delta z_{21}}}. \quad \text{(A.3)}$$

The analytical solution of Eq. (A.15) or Eq. (A.16) allows to retrieve the term B_{wat}. These above-mentioned equations are valid under the following assumptions:

- The contributions to the measured signal in bin 23 from sea surface back-scattering and from sea bottom reflection are negligeable;
- Sea surface transmittance independent from the direction of propagation: i.e. downward and upward;
- The difference between atmospheric back-scattering contribution of bin 22 and 23 is negligible compared to the contribution of sea water in bin 23;
- Atmospheric back-scattering dominated by molecular contribution both for the optical thickness as well as for the shape of the phase function;
- homogeneity of the aerosol type in the MABL and known vertical distribution.

Practically, from Eq. (A.15) or Eq. (A.16) it is possible to estimate B_{wat} if, in addition to the range corrected signals at bin 21, 22 and 23 (S_{21}^*,S_{22}^* and S_{23}^*) and the corresponding geometry (Z_{21},Z_{22} and Z_{23}) are known the following variables:

- the refractive index of sea water n.
- sea surface trasmittance T_s^2 that depends from the sea surface roughness. Assuming that, for ALADIN geometry, the dependence of sea surface roughness from surface (2 or 10 m) wind can be neglected, a constant value of 0.97 can be adopted (Churnside, 2013).
- Molecular scattering properties that can be easily estimated knowing the atmospheric density profile (i.e. p, T profile) in the range of interest (~0,1500 m). The required information on the density profile can be obtained by ancillary data (e.g. model forecasts or reanalyses).
- Marine boundary layer aerosols properties: density at the surface (ρ_0), extinction at laser emission wavelength (σ_{ext}) and scale height or any information on the vertical distribution (z_s). Aerosols information can be obtained from climatology, models or, if available, from Aeolus derived aerosols product.

Appendix B

The dominant source of uncertainty is the radiometric noise. The uncertainty on the final product ΔB_{wat} is estimated quantitatively by applying the error propagation formula to the analytical solution of Eq. assuming only the radiometric noise as the uncertainty source:

$$\Delta B_{wat}(355) = \sqrt{\left(\frac{\partial B_{wat}}{dS_{21}^*} \right)^2 \bullet \left(\Delta S_{21}^*\right)^2 + \left(\frac{\partial B_{wat}}{dS_{22}^*} \right)^2 \bullet \left(\Delta S_{22}^*\right)^2 + \left(\frac{\partial B_{wat}}{dS_{23}^*} \right)^2 \bullet \left(\Delta S_{23}^*\right)^2}, \quad \text{(B.1)}$$

where:

$$\frac{\partial B_{wat}}{dS_{21}^{*}} = C \bullet \frac{(k+1) \bullet \left(S_{22}^{*\ (k+1)} - S_{23}^{*} \bullet S_{22}^{*\ k}\right)}{S_{21}^{*\ (k+2)}}; \tag{B.2}$$

$$\frac{\partial B_{wat}}{dS_{22}^{*}} = C \bullet \frac{k \bullet S_{23}^{*} \bullet S_{22}^{*\ (k-1)} - (k+1) \bullet S_{22}^{*\ k}}{S_{21}^{*\ (k+2)}}; \tag{B.3}$$

$$\frac{\partial B_{wat}}{dS_{23}^{*}} = C \bullet \frac{S_{22}^{*\ k}}{S_{21}^{*\ (k+1)}}; \tag{B.4}$$

$$k = \left(-\frac{e^{\frac{z_{21}}{z_s}}}{\Delta z_{21}}\right)\left(e^{\frac{-z_{21}}{z_s}}\Delta z_{21} + e^{\frac{-z_{22}}{z_s}}\Delta z_{22} + e^{\frac{-z_{23}}{z_s}}\Delta z_{23}\right); \tag{B.5}$$

$$C = \left(\frac{B_{21m}n^2}{T_s^2 T_{BLm}^2}\right) \bullet \left(\frac{B_{21m}}{B_{22m}}\frac{1}{T_{21m}^2}\right)^{k}. \tag{B.6}$$

The values for the uncertainty associated with the S_{21}^{*}, S_{22}^{*} and S_{23}^{*} are obtained from the SNR as distributed from L1B Aeolus data accounting for range correction. For the meaning of the notation used in eqs. B.4-B.6, please refer to Section 4.2.

References

Argo float data and metadata from Global Data Assembly Centre (Argo GDAC), 2023. [Dataset]. SEANOE. Available at: ftp://ftp.ifremer.fr/ifremer/argo (Accessed: 2023/12). 10.17882/42182.

Behrenfeld, M.J., Hu, Y., Hostetler, C.A., Dall'Olmo, G., Rodier, S.D., Hair, J.W., Trepte, C.R., 2013. Space-based lidar measurements of global ocean carbon stocks. Geophys. Res. Lett. 40, 4355–4360. https://doi.org/10.1002/grl.50816.

Behrenfeld, M.J., Gaube, P., Della Penna, A., O'Malley, R.T., Burt, W.J., Hu, Y., Bontempi, P.S., Steinberg, D.K., Boss, E.S., Siegel, D.A., Hostetler, C.A., Tortell, P.D., Doney, S.C., 2019. Global satellite-observed daily vertical migrations of ocean animals. Nature 576, 257–261. https://doi.org/10.1038/s41586-019-1796-9.

Behrenfeld, M.J., Lorenzoni, L., Hu, Y., Bisson, K.M., Hostetler, C.A., Di Girolamo, P., Dionisi, D., Longo, F., Zoffoli, S., 2023. Satellite Lidar measurements as a critical new Global Ocean climate record. Remote Sens. (Basel) 15, 5567. https://doi.org/10.3390/rs15235567.

Bodhaine, B.A., Wood, N.B., Dutton, E.G., Slusser, J.R., 1999. On Rayleigh optical depth calculations. J. Atmos. Oceanic Tech. 16, 1854–1861. https://doi.org/10.1175/1520-0426(1999)016<1854:ORODC>2.0.CO;2.

Bricaud, A., Babin, M., Claustre, H., Ras, J., Tièche, F., 2010. Light absorption properties and absorption budget of Southeast Pacific waters. J. Geophys. Res. Oceans 115. https://doi.org/10.1029/2009JC005517.

Churnside, J.H., 2013. Review of Profiling Oceanographic Lidar. OE, 53. https://doi.org/10.1117/1.OE.53.5.051405, 051405.

Dabas, A., 2017. Generation of AUX_CAL, Detailed Processing Model, Input/Output Data Definition.

D'Alimonte, D., Kajiyama, T., Liberti, G.L., Di Paolantonio, M., Franco, N., Di Girolamo, P., Dionisi, D., 2024. In-water lidar simulations: the ALADIN ADM-Aeolus backscattered signal at 355 nm. Optics Express, 32, 22781 - 22803. doi: 10.1364/OE.510919. In: .

Di Girolamo, P., Franco, N., Dionisi, D., Di Paolantonio, M., Summa, D., Lolli, S., Mona, L., Santoleri, R., Zoffoli, S., Tataranni, F., Scopa, T., Longo, F., Votta, R., Sacchieri, V., Perna, A., Cosentino, A., Hu, Y., Behrenfeld, M.J., Hostetler, C.A., Hall, S.R., Trepte, C.R., 2024. The cloud and aerosol Lidar for global scale observations of the ocean-land-atmosphere system – CALIGOLA. Bull. Am. Meteorol. Soc. (in preparation).

Dionisi, D., Brando, V.E., Volpe, G., Colella, S., Santoleri, R., 2020. Seasonal distributions of ocean particulate optical properties from spaceborne lidar measurements in Mediterranean and Black Sea. Remote Sens. Environ. 247, 111889 https://doi.org/10.1016/j.rse.2020.111889.

Donovan, D., van Zadelhoff, G.-J., Wang, P., Huber, D., 2021. ATILD cloud/aerosol algorithms applied to ALADIN (no. EGU21-15189). In: Presented at the EGU21, Copernicus Meetings. https://doi.org/10.5194/egusphere-egu21-15189.

Ehlers, F., Flament, T., Dabas, A., Trapon, D., Lacour, A., Baars, H., Straume-Lindner, A. G., 2022. Optimization of Aeolus' aerosol optical properties by maximum-likelihood estimation. Atmos. Meas. Tech. 15, 185–203. https://doi.org/10.5194/amt-15-185-2022.

Flament, T., Trapon, D., Lacour, A., Dabas, A., Ehlers, F., Huber, D., 2021. Aeolus L2A aerosol optical properties product: standard correct algorithm and Mie correct algorithm. Atmos. Meas. Tech. 14, 7851–7871. https://doi.org/10.5194/amt-14-7851-2021.

Hostetler, C.A., Behrenfeld, M.J., Hu, Y., Hair, J.W., Schulien, J.A., 2018. Spaceborne Lidar in the study of marine systems. Ann. Rev. Mar. Sci. 10, 121–147. https://doi.org/10.1146/annurev-marine-121916-063335.

Illingworth, A.J., Barker, H.W., Beljaars, A., Ceccaldi, M., Chepfer, H., Clerbaux, N., Cole, J., Delanoë, J., Domenech, C., Donovan, D.P., Fukuda, S., Hirakata, M., Hogan, R.J., Huenerbein, A., Kollias, P., Kubota, T., Nakajima, T., Nakajima, T.Y., Nishizawa, T., Ohno, Y., Okamoto, H., Oki, R., Sato, K., Satoh, M., Shephard, M.W., Velázquez-Blázquez, A., Wandinger, U., Wehr, T., Van Zadelhoff, G.-J., 2015. The EarthCARE satellite: the next step forward in global measurements of clouds, aerosols, precipitation, and radiation. Bull. Am. Meteorol. Soc. 96, 1311–1332. https://doi.org/10.1175/BAMS-D-12-00227.1.

Jamet, C., Ibrahim, A., Ahmad, Z., Angelini, F., Babin, M., Behrenfeld, M.J., Boss, E., Cairns, B., Churnside, J., Chowdhary, J., Davis, A.B., Dionisi, D., Duforêt-Gaurier, L., Franz, B., Frouin, R., Gao, M., Gray, D., Hasekamp, O., He, X., Hostetler, C., Kalashnikova, O.V., Knobelspiesse, K., Lacour, L., Loisel, H., Martins, V., Rehm, E., Remer, L., Sanhaj, I., Stamnes, K., Stamnes, S., Victori, S., Werdell, J., Zhai, P.-W., 2019. Going beyond Standard Ocean color observations: Lidar and polarimetry. Front. Mar. Sci. 6, 251. https://doi.org/10.3389/fmars.2019.00251.

Jutard, Q., Organelli, E., Briggs, N., Xing, X., Schmechtig, C., Boss, E., Poteau, A., Leymarie, E., Cornec, M., D'Ortenzio, F., Claustre, H., 2021. Correction of biogeochemical-Argo radiometry for sensor temperature-dependence and drift: protocols for a delayed-mode quality control. Sensors 6217 (21), 19. https://doi.org/10.3390/s21186217.

Kim, G.E., Gnanadesikan, A., Del Castillo, C.E., Pradal, M.-A., 2018. Upper Ocean cooling in a coupled climate model due to light attenuation by yellowing materials. Geophys. Res. Lett. https://doi.org/10.1029/2018GL077297.

Lee, Z.P., Carder, K.L., Chen, R.F., Peacock, T.G., 2002. Deriving inherent optical properties from water color: a multiband quasi-analytical algorithm for optically deep waters. Appl. Optics 41, 5755–5772.

Lee, Z.P., Hu, C., Shang, S., Du, K., Lewis, M., Arnone, R., Brewin, R., 2013. Penetration of UV-visible solar radiation in the global oceans: insights from ocean color remote sensing. J. Geophys. Res. Oceans 118, 4241–4255.

Li, H., He, X., Ding, J., Bai, Y., Wang, D., Gong, F., Li, T., 2022. The inversion of HY-1C-COCTS Ocean color remote sensing products from high-latitude seas. Remote Sens. (Basel) 14, 5722. https://doi.org/10.3390/rs14225722.

Loew, A., Bell, W., Brocca, L., Bulgin, C.E., Burdanowitz, J., Calbet, X., Donner, R.V., Ghent, D., Gruber, A., Kaminski, T., Kinzel, J., Klepp, C., Lambert, J.-C., Schaepman-Strub, G., Schröder, M., Verhoelst, T., 2017. Validation practices for satellite-based earth observation data across communities. Rev. Geophys. 55, 779–817. https://doi.org/10.1002/2017RG000562.

Lu, X., Hu, Y., Yang, Y., Bontempi, P., Omar, A., Baize, R., 2020. Antarctic spring ice-edge blooms observed from space by ICESat-2. Remote Sens. Environ. 245 https://doi.org/10.1016/j.rse.2020.111827 undefined-undefined.

Lu, X., Hu, Y., Omar, A., Baize, R., Vaughan, M., Rodier, S., Kar, J., Getzewich, B., Lucker, P., Trepte, C., Hostetler, C., Winker, D., 2021. Global Ocean studies from CALIOP/CALIPSO by removing polarization crosstalk effects. Remote Sens. (Basel) 13, 2769. https://doi.org/10.3390/rs13142769.

Lu, X., Hu, Y., Omar, A., Yang, Y., Vaughan, M., Rodier, S., Garnier, A., Ryan, R., Getzewich, B., Trepte, C., 2022. Nearshore bathymetry and seafloor property studies from space lidars: CALIPSO and ICESat-2. Opt. Express, OE 30, 36509–36525. https://doi.org/10.1364/OE.471444.

Lu, X., Hu, Y., Omar, A., Yang, Y., Vaughan, M., Lee, Z., Neumann, T., Trepte, C., Getzewich, B., 2023. Lidar attenuation coefficient in the global oceans: insights from ICESat-2 mission. Opt. Express, OE 31, 29107–29118. https://doi.org/10.1364/OE.498053.

Mobley, C., Boss, E., Roesler, C., 2021. Ocean Optics Web Book [WWW document]. https://www.oceanopticsbook.info/.

Morel, A., Claustre, H., Antoine, D., Gentili, B., 2007. Natural variability of bio-optical properties in case 1 waters: attenuation and reflectance within the visible and near-UV spectral domains, as observed in South Pacific and Mediterranean waters. Biogeosciences 4, 913–925. https://doi.org/10.5194/bg-4-913-2007.

Nelson, N.B., Siegel, D.A., 2013. The global distribution and dynamics of Chromophoric dissolved organic matter. Ann. Rev. Mar. Sci. 5, 447–476. https://doi.org/10.1146/annurev-marine-120710-100751.

Nelson, N.B., Siegel, D.A., Michaels, A.F., 1998. Seasonal dynamics of colored dissolved material in the Sargasso Sea. Deep-Sea Res. I Oceanogr. Res. Pap. 45, 931–957. https://doi.org/10.1016/S0967-0637(97)00106-4.

Oelker, J., Losa, S.N., Richter, A., Bracher, A., 2022. TROPOMI-retrieved underwater light attenuation in three spectral regions in the ultraviolet and blue. Front. Mar. Sci. 9, 787992 https://doi.org/10.3389/fmars.2022.787992.

Organelli, E., Claustre, H., 2019. Small phytoplankton shapes colored dissolved organic matter dynamics in the North Atlantic subtropical gyre. Geophys. Res. Lett. 46, 12183–12191. https://doi.org/10.1029/2019GL084699.

Organelli, E., Claustre, H., Bricaud, A., Schmechtig, C., Poteau, A., Xing, X., Prieur, L., D'Ortenzio, F., Dall'Olmo, G., Vellucci, V., 2016. A novel near-real-time quality-control procedure for radiometric profiles measured by bio-Argo floats: protocols and performances. J. Atmos. Oceanic Tech. 33, 937–951. https://doi.org/10.1175/JTECH-D-15-0193.1.

Organelli, E., Claustre, H., Bricaud, A., Barbieux, M., Uitz, J., D'Ortenzio, F., Dall'Olmo, G., 2017. BIO-optical anomalies in the world's oceans: an investigation on the diffuse attenuation coefficients for downward irradiance derived from biogeochemical Argo float measurements: WORLD'S OCEAN BIO-OPTICAL ANOMALIES. J. Geophys. Res. Oceans 122, 3543–3564. https://doi.org/10.1002/2016JC012629.

Pitarch, J., 2017. Biases in ocean color over a Secchi disk. Opt. Express 25, A1124. https://doi.org/10.1364/OE.25.0A1124.

Qiu, J., Zong, X., Zhang, X., 2005. A study of the scaling height of the tropospheric aerosol and its extinction coefficient profile. J. Aerosol Sci. 36, 361–371. https://doi.org/10.1016/j.jaerosci.2004.10.005.

Reitebuch, O., Lemmerz, C., Nagel, E., Paffrath, U., Durand, Y., Endemann, M., Fabre, F., Chaloupy, M., 2009. The airborne demonstrator for the direct-detection Doppler wind Lidar ALADIN on ADM-Aeolus. Part I: instrument design and comparison to satellite instrument. J. Atmos. Oceanic Tech. 26, 2501–2515. https://doi.org/10.1175/2009JTECHA1309.1.

Reitebuch, O., Huber, D., Nikolaus, I., 2018. ADM-Aeolus Algorithm Theoretical Basis Document ATBD Level1B Products.

Rennie, M., Isaksen, L., 2020. The NWP impact of Aeolus level-2B winds at ECMWF. ECMWF technical. In: Memorandum No. 864.

Rennie, M.P., Isaksen, L., Weiler, F., de Kloe, J., Kanitz, T., Reitebuch, O., 2021. The impact of Aeolus wind retrievals on ECMWF global weather forecasts. Q. J. Roy. Meteorol. Soc. 147, 3555–3586. https://doi.org/10.1002/qj.4142.

Röttgers, R., Doerffer, R., McKee, D., Schönfeld, W., 2016. The water optical properties processor (WOPP) pure water spectral absorption, scattering, and real part of refractive index model (algorithm theoretical basis document (ATBD) no. 1.8). In: ESA/ESRIN.

Sathyendranath, S., Brewin, R.J.W., Brockmann, C., Brotas, V., Calton, B., Chuprin, A., Cipollini, P., Couto, A.B., Dingle, J., Doerffer, R., Donlon, C., Dowell, M., Farman, A., Grant, M., Groom, S., Horseman, A., Jackson, T., Krasemann, H., Lavender, S., Martinez-Vicente, V., Mazeran, C., Mélin, F., Moore, T.S., Müller, D., Regner, P., Roy, S., Steele, C.J., Steinmetz, F., Swinton, J., Taberner, M., Thompson, A., Valente, A., Zühlke, M., Brando, V.E., Feng, H., Feldman, G., Franz, B.A., Frouin, R., Gould, R.W., Hooker, S.B., Kahru, M., Kratzer, S., Mitchell, B.G., Muller-Karger, F.E., Sosik, H.M., Voss, K.J., Werdell, J., Platt, T., 2019. An ocean-colour time series for use in climate studies: the experience of the ocean-colour climate change initiative (OC-CCI). Sensors 19, 4285. https://doi.org/10.3390/s19194285.

Siegel, D.A., Michaels, A.F., 1996. Quantification of non-algal light attenuation in the Sargasso Sea: implications for biogeochemistry and remote sensing. Deep-Sea Res. II Top. Stud. Oceanogr. 43, 321–345. https://doi.org/10.1016/0967-0645(96)00088-4.

Smyth, T.J., 2011. Penetration of UV irradiance into the global ocean. J. Geophys. Res. Oceans 116. https://doi.org/10.1029/2011JC007183.

Stoffelen, A., Pailleux, J., Källén, E., Vaughan, J.M., Isaksen, L., Flamant, P., Wergen, W., Andersson, E., Schyberg, H., Culoma, A., Meynart, R., Endemann, M., Ingmann, P., 2005. The atmospheric dynamics mission for global wind field measurement. Bull. Amer. Meteor. Soc. 86, 73–88. https://doi.org/10.1175/BAMS-86-1-73.

Terzić, E., Miró, A., Organelli, E., Kowalczuk, P., D'Ortenzio, F., Lazzari, P., 2021. Radiative transfer modeling with biogeochemical-Argo float data in the Mediterranean Sea. JGR Oceans 126. https://doi.org/10.1029/2021JC017690.

Tsai, T.-C., Jeng, Y.-J., Chu, D.A., Chen, J.-P., Chang, S.-C., 2011. Analysis of the relationship between MODIS aerosol optical depth and particulate matter from 2006 to 2008. Atmos. Environ. 45, 4777–4788. https://doi.org/10.1016/j.atmosenv.2009.10.006.

Vadakke-Chanat, S., Jamet, C., 2023. Validation protocol for the evaluation of space-borne lidar particulate back-scattering coefficient bbp. Frontiers in Remote Sensing 4.

Wang, Y., Lee, Z., Wei, J., Shang, S., Wang, M., Lai, W., 2021. Extending satellite ocean color remote sensing to the near-blue ultraviolet bands Remote Sens. Environ. 253.

Watkins, R.H., Sayers, M.J., Shuchman, R.A., Bosse, K.R., 2023. Assessment of using spaceborne LiDAR to monitor the particulate backscatter coefficient on large, freshwater lakes: a test using CALIPSO on Lake Michigan. Frontiers in Remote Sensing 4.

Weiler, F., Rennie, M., Kanitz, T., Isaksen, L., Checa, E., de Kloe, J., Okunde, N., Reitebuch, O., 2021. Correction of wind bias for the lidar on board Aeolus using telescope temperatures. Atmos. Meas. Tech. 14, 7167–7185. https://doi.org/10.5194/amt-14-7167-2021.

Werdell, P.J., Behrenfeld, M.J., Bontempi, P.S., Boss, E., Cairns, B., Davis, G.T., Franz, B. A., Gliese, U.B., Gorman, E.T., Hasekamp, O., Knobelspiesse, K.D., Mannino, A., Martins, J.V., McClain, C.R., Meister, G., Remer, L.A., 2019. The plankton, aerosol, cloud, ocean ecosystem Mission: status, science, advances. Bull. Am. Meteorol. Soc. 100, 1775–1794. https://doi.org/10.1175/BAMS-D-18-0056.1.

Winker, D.M., Couch, R.H., McCormick, M.P., 1996. An overview of LITE: NASA's Lidar in-space technology experiment. Proc. IEEE 84, 164–180. https://doi.org/10.1109/5.482227.

Yang, J., Zheng, H., Ma, Y., Zhao, P., Zhou, H., Li, S., Wang, X.H., 2023. Background noise model of spaceborne photon-counting lidars over oceans and aerosol optical depth retrieval from ICESat-2 noise data. Remote Sens. Environ. 299, 113858 https://doi.org/10.1016/j.rse.2023.113858.

Zhang, S., Chen, P., Zhang, Z., Pan, D., 2022. Carbon Air–Sea Flux in the Arctic Ocean from CALIPSO from 2007 to 2020. Remote Sens. (Basel) 14, 6196. https://doi.org/10.3390/rs14246196.

Zhang, Z., Chen, P., Jamet, C., Dionisi, D., Hu, Y., Lu, X., Pan, D., 2023a. Retrieving bbp and POC from CALIOP: a deep neural network approach. Remote Sens. Environ. 287, 113482 https://doi.org/10.1016/j.rse.2023.113482.

Zhang, Z., Chen, P., Zhong, C., Xie, C., Sun, M., Zhang, S., Chen, S., Wu, D., 2023b. Chlorophyll and POC in polar regions derived from spaceborne lidar. Frontiers in marine. Science 10.

Zhang, S., Chen, P., Hu, Y., Zhang, Z., Jamet, C., Lu, X., Dionisi, D., Pan, D., 2024. Research ReportDiurnal global ocean surface pCO2 and air–sea CO2 flux reconstructed from spaceborne LiDAR data. PNAS Nexus 3, pgad432. https://doi.org/10.1093/pnasnexus/pgad432.